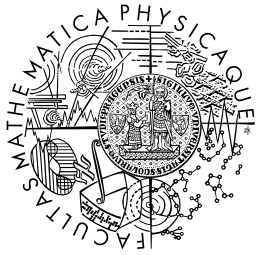

FACULTY
OF MATHEMATICS
AND PHYSICS
Charles University

MASTER THESIS

Jan Hrůza

Numerical simulations of interaction between fluid flow and rigid particles

Mathematical Institute of Charles University

Supervisor of the master thesis: RNDr. Karel Tůma, Ph.D.

Study programme: Mathematical Modelling in Physics and Engineering

Prague 2022

I declare that I carried out this master thesis independently, and only with the cited sources, literature and other professional sources. It has not been used to obtain another or the same degree.

I understand that my work relates to the rights and obligations under the Act No. 121/2000 Sb., the Copyright Act, as amended, in particular the fact that the Charles University has the right to conclude a license agreement on the use of this work as a school work pursuant to Section 60 subsection 1 of the Copyright Act.

In ..... date ....

Author's signature

I would like to express my appreciation to my supervisor RNDr. Karel Tůma, Ph.D. for the guidance throughout the work. On top of that, I would like to thank Jakub Fara for the access to the `admesh` library and my partner Adéla for limitless support during my studies.

Title: Numerical simulations of interaction between fluid flow and rigid particles

Author: Jan Hrůza

Institute: Mathematical Institute of Charles University

Supervisor: RNDr. Karel Tůma, Ph.D., Mathematical Institute of Charles University

Abstract: The thesis describes the implementation of a numerical model that simulates the interaction between rigid particles and a fluid. The numerical model is based on the arbitrary Lagrangian-Eulerian (ALE) method, which uses the movement of the mesh to realize the movement of particles. The ALE method is initially presented on a simple problem of calculating the drag force acting on a single sphere moving through a viscous fluid. A general version of the model capable of simulating tens of particles is then described and tested on various benchmarks to prove the reliability of used method. Finally, a problem inspired by the flow of red blood cells in the blood is studied to show the effect of shear thinning emerging in a mixture of Newtonian fluid and rigid particles.

Keywords: finite element method, arbitrary Lagrangian-Eulerian method, fluid-rigid solid interaction

Contents

Introduction

Our aim is to describe the interactions between rigid particles and fluid flow. As we deal with a mixture of a liquid and solids, one may perceive this problem from a point of view of mixture theory, which gives us a description of various complicated systems. The examples of such systems are solid particles submerged in a liquid, a chemical reaction in a fluid mixture, flow of water through a porous media, or various phase transitions. In all previously mentioned examples, tools of continuum mechanics can be used to derive a system of partial differential equations describing the mixture as a whole. This may not always be the most suitable approach as for example the submerged particles may be too large to be considered a part of the fluid in the model. We focus on a method that directly solves the problem of interaction between fluid flow and relatively large rigid particles that are described on individual level.

Let us consider another example, blood is a liquid composed of liquid blood plasma and red blood cells, other components are neglected for this example. The blood as a whole is known to show the non-Newtonian effect of shear thinning due to complicated interactions between red blood cells as described in Lanotte et al. [2016]. The flow of blood including the shear thinning effect can be described by variety of different models as presented by Trdlicová [2021]. Our aim is to show, that it is possible to replicate this behavior with a system of individual rigid particles submerged in a Newtonian fluid. We show that this system as a whole possesses the shear thinning property, although the fluid itself does not.

To obtain a numerical solution, we use the finite element method to discretize the solution in space. We chose to use the arbitrary Lagrangian-Eulerian (ALE) method for the particle motion as presented in Hu et al. [2001] to simulate tens of large particles with a high precision. As an alternative method, well suited for larger number of particles, the fictitious boundary method as described by Wan and Turek [2006] could be used for this problem. The ALE method is based on cutting out the particles from computational domain, prescribing the equation of rigid motion to the particle and coupling the particle movement with the fluid movement via boundary conditions. In each step, the computational domain is thus moved according to particle movement.

To study the shear thinning properties of the mixture, we define the concept of apparent viscosity to compare the response of the fluid-particle mixture to the response of a pure Newtonian fluid. This method was used in Lefebvre and Maury [2005] to investigate the dependence of the apparent viscosity of a fluid-particle mixture under shear stress on various parameters, specifically the particle distribution, interaction forces and the solid fraction. However, no investigation of shear thinning, or the influence of shear rate magnitude on the apparent viscosity in general, was done in this paper.

1. Stokes formula benchmark for ALE method

In this chapter we show the calculation of a drag acting on a sphere moving through a viscous incompressible Navier-Stokes fluid in an infinitely large domain. For small values of Reynolds number, the drag forces are given by the Stokes formula. This formula can be used as a benchmark for two types of numerical computations. In the first example we assume the sphere is stationary and the fluid moves, on the contrary in the second example we move the sphere using ALE (arbitrary Lagrangian-Eulerian) method in a stationary fluid. Our aim is to present ALE method on a simple example, which gives us a good starting point for generalization presented in the following chapter.

1.1 Problem description

Let us consider a sphere submerged in an infinitely large volume of a still viscous fluid moving in uniform linear motion. We denote the velocity of the sphere with $\mathbf{V}$. This setup and the resulting forces are equivalent to a problem, where the sphere is stationary and the fluid moves with a velocity $-\mathbf{V}$ instead. In this case the fluid velocity is considered in an infinite distance from the sphere. This leads us to the following formulation of the problem.

Let Ω be a sphere in $\mathbb{R}^3$ with the center in the origin and the radius R. We want to find a functions $\mathbf{v} : (0,T) \times \mathbb{R}^3 \setminus \Omega \to \mathbb{R}^3$ and $p : (0,T) \times \mathbb{R}^3 \setminus \Omega \to \mathbb{R}$ fulfilling the incompressible homogeneous Navier-Stokes equations

$$\rho\left(\frac{\partial}{\partial t}\mathbf{v} + (\mathbf{v}\cdot\nabla)\,\mathbf{v}\right) = \operatorname{div}\mathbb{T} \qquad \text{in } \mathbb{R}^3 \setminus \Omega, \tag{1.1}$$

$$\operatorname{div}\mathbf{v} = 0 \qquad \text{in } \mathbb{R}^3 \setminus \Omega, \tag{1.2}$$

$$\mathbb{T} = -p\mathbb{I} + \mu\left(\nabla\mathbf{v} + (\nabla\mathbf{v})^T\right), \tag{1.3}$$

where $\mu > 0$ is the dynamic viscosity and $\rho > 0$ is the fluid density. Throughout the thesis, we use the notation $\mathbb{D} = \frac{1}{2}\left(\nabla\mathbf{v} + (\nabla\mathbf{v})^T\right)$ for the symmetric gradient. We demand that $\mathbf{v}$ satisfies the following boundary conditions

$$\mathbf{v} = \mathbf{0} \quad \text{on } \partial\Omega, \tag{1.4}$$

$$\mathbf{v} \xrightarrow[\|x\|\to\infty]{} \mathbf{V} \in \mathbb{R}^3. \tag{1.5}$$

We further assume, without loss of generality, that $\mathbf{V} = (V, 0, 0)$ is non-zero only in the direction of the x coordinate axis. The use of this assumption is correct due to spherical symmetry of the domain.

1.2 Analytical solution

In this section we present the method of obtaining the analytical solution of the problem above presented by Brdička [2005]. To obtain explicit formula, we

assume the Reynolds number is very small, i.e.

$$\mathrm{Re} = \frac{VR\rho}{\mu} \ll 1.$$

With this assumption we use the approximation of the convective term in the balance of linear momentum equation (1.1)

$$\mathbf{v} \cdot \nabla \mathbf{v} \approx \mathbf{V} \cdot \nabla \mathbf{v}.$$

Using this approximation, we simplify the problem to a linear partial differential equation, the equations resulting from this approximation is often referred to as Oseen equations. Omitting the convective term completely would lead to Stokes equations. The problem is axially symmetric, therefore the solution should be axially symmetric and should be identical in any plane that contains the x coordinate axis. Let us define the spherical coordinates with variables (r, θ, φ), where $r \in [0, \infty)$ is the distance from origin, $\theta \in [0, \pi]$ is the angle between the given vector and the x coordinate vector and $\varphi \in [0, 2\pi)$ is the azimuthal angle of rotation around x axis. The previously stated assumption means that $\mathbf{v}$ does not depend on φ. We can further assume no flow in the φ-direction $v_\varphi = 0$. Altogether we assume

$$v_r = v_r(r, \theta), \quad v_\theta = v_\theta(r, \theta), \quad v_\varphi = 0, \quad p = p(r, \theta). \tag{1.6}$$

As the next step we formulate the Navier-Stokes equations in spherical coordinates. The balance of linear momentum equations are in the following form

$$\begin{aligned}
&\frac{\partial v_r}{\partial t} + v_r \frac{\partial v_r}{\partial r} + \frac{v_\theta}{r}\frac{\partial v_r}{\partial \theta} + \frac{v_\varphi}{r\sin\theta}\frac{\partial v_r}{\partial \varphi} - \frac{v_\theta^2 + v_\varphi^2}{r} = \\
&= -\frac{1}{\rho}\frac{\partial p}{\partial r} + \nu\left(\frac{1}{r}\frac{\partial^2 (r v_r)}{\partial r^2} + \frac{1}{r^2}\frac{\partial^2 v_r}{\partial \theta^2} + \frac{1}{r^2\sin^2\theta}\frac{\partial^2 v_r}{\partial \varphi^2} + \frac{\cot\theta}{r^2}\frac{\partial v_r}{\partial \theta} - \frac{2}{r^2}\frac{\partial v_\theta}{\partial \theta} - \right. \\
&\quad \left. - \frac{2}{r^2\sin\theta}\frac{\partial v_\varphi}{\partial \varphi} - \frac{2v_r}{\varphi} - \frac{2v_\varphi^2\cot}{r}\right), \\
&\frac{\partial v_\theta}{\partial t} + v_r \frac{\partial v_\theta}{\partial \theta} + \frac{v_\theta}{r}\frac{\partial v_\theta}{\partial \varphi} + \frac{v_\varphi}{r\sin\theta}\frac{\partial v_\theta}{\partial \varphi} + \frac{v_r v_\theta}{r} - \frac{v_\varphi^2\cot\theta}{r} = \\
&= -\frac{1}{\rho r}\frac{\partial p}{\partial \theta} + \nu\left(\frac{1}{r}\frac{\partial^2 (r v_\theta)}{\partial r^2} + \frac{1}{r^2}\frac{\partial^2 v_\theta}{\partial \theta^2} + \frac{1}{r^2\sin^2\theta}\frac{\partial^2 v_\theta}{\partial \varphi^2} + \frac{\cot\theta}{r^2}\frac{\partial v_\theta}{\partial \theta} - \right. \\
&\quad \left. - \frac{2\cos\theta}{r^2\sin^2\theta}\frac{\partial v_\varphi}{\partial \varphi} + \frac{2}{r^2}\frac{\partial v_r}{\partial \theta} - \frac{v_\theta}{r^2\sin^2\theta}\right), \\
&\frac{\partial v_\varphi}{\partial t} + v_r \frac{\partial v_\varphi}{\partial r} + \frac{v_\theta}{r}\frac{\partial v_\varphi}{\partial \theta} + \frac{v_\varphi}{r\sin\theta}\frac{\partial v_\varphi}{\partial \varphi} + \frac{v_r v_\varphi}{t} + \frac{v_\theta v_\varphi\cot\theta}{r} = \\
&= -\frac{1}{\rho r\sin\theta}\frac{\partial p}{\partial \varphi} + \nu\left(\frac{1}{r}\frac{\partial^2 (r v_\varphi)}{\partial r^2} + \frac{1}{r^2}\frac{\partial^2 v_\varphi}{\partial \theta^2} + \frac{1}{r^2\sin^2\theta}\frac{\partial^2 v_\varphi}{\partial \varphi^2} + \frac{\cot\theta}{r^2}\frac{\partial v_\varphi}{\partial \theta} + \right. \\
&\quad \left. + \frac{2}{r^2\sin\theta}\frac{\partial v_r}{\partial \varphi} + \frac{2\cos\theta}{r^2\sin^2\theta}\frac{\partial v_\theta}{\partial \varphi} - \frac{v_\varphi}{r^2\sin^2\theta}\right).
\end{aligned}$$

The continuity equation is then in the form

$$\frac{\partial v_r}{\partial r} + \frac{1}{r}\frac{\partial v_\theta}{\partial \theta} + \frac{1}{r\sin\theta}\frac{\partial v_\varphi}{\partial \varphi} + \frac{2v_r}{r} + \frac{v_\theta\cot\theta}{t} = 0. \tag{1.7}$$

These equations simplify significantly due to (1.6)

$$\frac{\partial p}{\partial r} = \mu\left(\frac{\partial^2 v_r}{\partial r^2} + \frac{1}{r^2}\frac{\partial^2 v_r}{\partial \theta^2} + \frac{2}{r}\frac{\partial v_r}{\partial r} + \frac{\cot\theta}{r^2}\frac{\partial v_r}{\partial \theta} - \frac{2}{r^2}\frac{\partial v_\theta}{\partial \theta} - \frac{2v_r}{r^2} - \frac{2v_\theta\cot\theta}{r^2}\right), \tag{1.8}$$

$$\frac{1}{r}\frac{\partial p}{\partial \theta} = \mu\left(\frac{\partial^2 v_\theta}{\partial r^2} + \frac{1}{r^2}\frac{\partial^2 v\theta}{\partial \theta^2} + \frac{2}{r}\frac{\partial v_\theta}{\partial r} + \frac{\cot\theta}{r^2}\frac{\partial v_\theta}{\partial \theta} + \frac{2}{r^2}\frac{\partial v_r}{\partial \theta} - \frac{v_\theta}{r^2\sin^2\theta}\right), \tag{1.9}$$

$$0 = \frac{\partial v_r}{\partial r} + \frac{1}{r}\frac{\partial v_\theta}{\partial \theta} + \frac{2v_r}{r} + \frac{v_\theta\cot\theta}{r}. \tag{1.10}$$

The boundary conditions (1.4) and (1.5) in spherical coordinates transform to the following conditions for components

$$\begin{aligned} &v_r = V\cos\theta, && v_\theta = -V\sin\theta && \text{for } r\to\infty,\\ &v_r = 0, && v_\theta = 0 && \text{for } r = R. \end{aligned}$$

Now we assume that both functions v_r and v_θ can be represented as a product of a function depending only on r and a function depending only on θ. Moreover, in accordance with the boundary conditions, let us assume

$$v_r = F(r)\cos\theta, \quad v_\theta = G(r)\sin\theta. \tag{1.11}$$

The functions F and G have to fullfill

$$F(r) \xrightarrow[r\to\infty]{} V, \quad G(r) \xrightarrow[r\to\infty]{} V, \quad F(R) = 0, \quad G(R) = 0.$$

By substituting (1.11) into (1.8) and (1.9) we obtain

$$\begin{aligned} \frac{\partial p}{\partial r} &= \mu\left(F'' + \frac{2}{r}F' - \frac{4}{r^2}F - \frac{4}{r^2}G\right)\cos\theta,\\ \frac{1}{r}\frac{\partial p}{\partial \theta} &= \mu\left(G'' + \frac{2}{r}G' - \frac{2}{r^2}G - \frac{2}{r^2}F\right)\sin\theta,\\ 0 &= \left(F' + \frac{2}{r}F + \frac{2}{r}G\right)\cos\theta. \end{aligned} \tag{1.12}$$

From the first two equations, we see that the pressure has to be in the form

$$p(r,\theta) = \mu H(r)\cos\theta.$$

We substitute this form of pressure into (1.12). The resulting equation have to hold for any θ, we can therefore focus on the part depending only on the variable r

$$H' = F'' + \frac{2}{r}F' - \frac{4}{r^2}F - \frac{4}{r^2}G, \tag{1.13}$$

$$H = G'' + \frac{2}{r}G' - \frac{2}{r^2}G - \frac{2}{r^2}F, \tag{1.14}$$

$$G = -\frac{r}{2}F' - F. \tag{1.15}$$

Using (1.15), we substitute G in (1.14) and obtain

$$H = \frac{r^2}{2}F''' + 3rF'' + 2F', \tag{1.16}$$

which after applying the derivative with respect to r gives

$$H' = \frac{r^2}{2} F^{(iv)} + 4rF''' + 5F''.$$

Now, we subtract (1.13) from this equation and multiply the result by $2r$ to obtain

$$0 = r^3 F^{(iv)} + 8r^2 F''' + 8rF'' - 8F'. \tag{1.17}$$

This ordinary differential equation is a homogenous Euler equation, and it can be easily solved assuming F is in the form $F = cr^n$ for some constant c. Substituting this general form of F in (1.17) results in

$$\begin{aligned}
0 &= (n(n-1)(n-2)(n-3) + 8n(n-1)(n-2) + 8n(n-1) - 8n)\, r^n, \\
0 &= n((n-1)(n-2)(n-3) + 8(n-1)(n-2) + 8(n-1) - 8), \\
0 &= n(n-2)(n^2 + 4n + 3), \\
0 &= n(n-2)(n+1)(n+3).
\end{aligned}$$

The general solution therefore reads

$$F(r) = A + \frac{B}{r} + \frac{C}{r^3} + Dr^2.$$

Using (1.15) and (1.16) we obtain the general form of G and H

$$\begin{aligned}
G(r) &= -Q - \frac{B}{2r} + \frac{C}{2r^3} - 2Dr^2, \\
H(r) &= \frac{B}{r^2} + 10Dr.
\end{aligned}$$

By passing to infinity in the previous equations, we obtain the relations for constants A and D

$$A = V, \quad D = 0.$$

With this result and the boundary conditions for $r = R$, we obtain

$$\begin{aligned}
V + \frac{1}{R} B + \frac{1}{R^3} C &= 0, \\
-V - \frac{1}{2R} B + \frac{1}{2R^3} C &= 0.
\end{aligned}$$

Overall, we obtained the exact form of all constants

$$Q = V, \quad B = -\frac{3}{2} RV, \quad C = \frac{1}{2} R^3 V, \quad D = 0.$$

With this final result, we obtained the velocity field describing the flow around the sphere

$$\begin{aligned}
v_r &= V \cos\theta \left(1 - \frac{3R}{2r} + \frac{R^3}{2r^3}\right), \\
v_\theta &= -V \sin\theta \left(1 - \frac{3R}{4r} - \frac{R^3}{4r^3}\right), \\
p &= -\frac{3\mu RV}{2r^2}.
\end{aligned} \tag{1.18}$$

The last step is to compute the drag force acting on the sphere. We therefore need to integrate the traction over the sphere surface, where the traction $\mathbf{t}$ is defined for surface with the unit outer normal vector $\mathbf{n}$ as

$$\mathbf{t} = \mathbb{T}\mathbf{n}. \tag{1.19}$$

The outer unit normal is equivalent to local unit vector in the direction of increasing r denoted by $\mathbf{e}_r$. We therefore only need to compute the elements T_{rr} and $T_{r\theta}$ of the Cauchy stress tensor $\mathbb{T}$, because from the form of the unit normal vector, we have

$$t_r = T_{rr}, \quad t_\theta = T_{r\theta}, \quad t_\varphi = T_{r\varphi} = 0.$$

The definition of the local coordinate basis of spherical coordinates gives

$$\mathbf{e}_x = \cos\theta \mathbf{e}_r - \sin\theta \mathbf{e}_\theta,$$

where $\mathbf{e}_\cdot$ are local coordinate vectors (unit vectors in the direction of increasing given coordinate). This implies a similar relation for the elements of traction $\mathbf{t}$

$$t_x = t_r \cos\theta - t_\theta \sin\theta = T_{rr}\cos\theta - T_{r\theta}\sin\theta.$$

Now let us use the solution (1.18) to compute this vector

$$\begin{aligned} T_{rr} &= -p + 2\mu\frac{\partial v_r}{\partial r} = \frac{3\mu V}{2R}\cos\theta, \\ T_{r\theta} &= \mu\left(\frac{1}{r}\frac{\partial v_r}{\partial \theta} + \frac{\partial v_\theta}{\partial r} - \frac{\partial v_\theta}{\partial r}\right) = -\frac{3\mu V}{2R}\sin\theta. \end{aligned}$$

Finally, we have everything we need to compute the drag force

$$\begin{aligned} F_d &= \int_{\partial\Omega} t_x \, dS = \int_0^\pi (T_{rr}\cos\theta - T_{r\theta}\sin\theta) 2\pi R^2 \sin\theta \, d\theta \\ &= 2\pi R^2 \int_0^\pi \frac{3\mu V}{2R}(\cos^2\theta + \sin^2\theta)\sin\theta \, d\theta \\ &= 3\pi\mu R V \int_0^\pi \sin\theta \, d\theta \\ &= 6\pi\mu R V. \end{aligned}$$

1.3 Numerical computation

To simplify the equations we take advantage of the cylindrical symmetry of the problem. We transition to cylindrical coordinates (x, r, φ)[1], where x is the x_1 coordinate, r is the distance from the x_1 axis and $\varphi \in [-\pi, \pi)$ is the angle defined as $cos(\varphi) = \frac{x_2}{r}$. The solution is axially symmetric around the x_1 axis, in other words, the solution only depends on x and r. We can therefore solve a much simpler two-dimensional problem instead of full three-dimensional one.

The major inconvenience with this problem is the infinite size of the domain with fluid. As working with the infinite domain is rather difficult numerically,

[1]The cylindrical coordinates are in a non-standard order to preserve the order of x coordinate, which is used instead of the usual z.

we use large, but finite, domain Ω_1 instead. The domain used in numerical computation is described in Figure 1.1. In this domain, we distinguish three parts of the boundary: The semi-circular part Γ_b corresponds to the sphere surface, we prescribe the no-slip boundary condition there. The outer part Γ_1 represents the "domain in infinite distance", the fluid movement is thus prescribed there. The remaining part Γ_0 lies on the axis of symmetry, the fluid only moves along this axis, thus we prescribe zero movement through this boundary, i.e. $v_r = 0$.

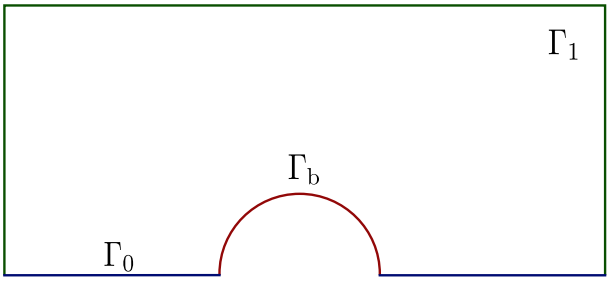

Figure 1.1: Boundary of the domain used in numerical computation. The domain is finite, with fixed width and height. Boundary velocity $\mathbf{V}$, originally demanded in infinity, is now prescribed on Γ_1. The surface of a sphere reduces in cylindrical coordinates to semicircle Γ_b.

1.3.1 Weak formulation

Let us now consider the cylindrical domain $\widetilde{\Omega}_1$ with a spherical hole defined by revolving Ω_1 around the x-axis. We denote the outer cylindrical boundary by $\widetilde{\Gamma}_1$ and the surface of the inner sphere by $\widetilde{\Gamma}_b$. We start with the Oseen approximation of equations (1.1) multiplied by sufficiently regular test functions $\tilde{\mathbf{v}} : \widetilde{\Omega}_1 \to \mathbb{R}^3$ and $\tilde{p} : \widetilde{\Omega}_1 \to \mathbb{R}$ respectively. Integrating over domain $\widetilde{\Omega}_1$ results in the following equations

$$\int_{\widetilde{\Omega}_1} \rho \left(\frac{\partial \mathbf{v}}{\partial t} + (\mathbf{V} \cdot \nabla)\mathbf{v} \right) \cdot \tilde{\mathbf{v}} \, dx - \int_{\widetilde{\Omega}_1} \operatorname{div}(\mathbb{T}) \, \tilde{\mathbf{v}} \, dx = 0, \tag{1.20}$$

$$\int_{\widetilde{\Omega}_1} \tilde{p} \operatorname{div} \mathbf{v} \, dx = 0. \tag{1.21}$$

Let us further assume that $\tilde{\mathbf{v}}$ vanishes on $\partial\widetilde{\Omega}_1$. Using this assumption and the Gauss divergence theorem, we obtain the identity

$$-\int_{\widetilde{\Omega}_1} (\operatorname{div} \mathbb{T}) \tilde{\mathbf{v}} \, dx = \int_{\widetilde{\Omega}_1} \mathbb{T} : \nabla \tilde{\mathbf{v}} \, dx, \tag{1.22}$$

where we define $\mathbb{A} : \mathbb{B} = \operatorname{Tr}\left(\mathbb{A}^T \mathbb{B}\right)$ for any two tensors $\mathbb{A}$, $\mathbb{B}$. Substituting this identity into (1.20) results in the following equation

$$\int_{\widetilde{\Omega}_1} \rho \left(\frac{\partial \mathbf{v}}{\partial t} + (\mathbf{V} \cdot \nabla)\mathbf{v} \right) \cdot \tilde{\mathbf{v}} \, dx + \int_{\widetilde{\Omega}_1} \mathbb{T} : \nabla \tilde{\mathbf{v}} \, dx = 0. \tag{1.23}$$

Using the assumption of cylindrical symmetry and the assumption of zero flow in the φ-direction we assume that the solution is in the form

$$\mathbf{v} = \begin{pmatrix} v_x(x,r) \\ v_r(x,r) \\ 0 \end{pmatrix}, \quad p = p(x,r).$$

The same assumptions are imposed on $\tilde{\mathbf{v}}$ as well. We proceed with expressing cylindrical forms of the differential operators that are significantly simplified by the assumptions on $\mathbf{v}$

$$\nabla\mathbf{v} = \begin{pmatrix} \frac{\partial v_x}{\partial x} & \frac{\partial v_x}{\partial r} & 0 \\ \frac{\partial v_r}{\partial x} & \frac{\partial v_r}{\partial r} & 0 \\ 0 & 0 & \frac{v_r}{r} \end{pmatrix}, \quad (\mathbf{v}\cdot\nabla)\mathbf{v} = \begin{pmatrix} V\frac{\partial v_x}{\partial x} \\ V\frac{\partial v_z}{\partial x} \\ 0 \end{pmatrix},$$

$$\begin{aligned} \mathbb{T} : \nabla\tilde{\mathbf{v}} = &-p\left(\frac{\partial \tilde{v}_x}{\partial x} + \frac{\partial \tilde{v}_r}{\partial r} + \frac{\tilde{v}_r}{r}\right) + \\ &+ 2\mu \begin{pmatrix} \frac{\partial v_x}{\partial x} & \frac{1}{2}\left(\frac{\partial v_x}{\partial r} + \frac{\partial v_r}{\partial x}\right) \\ \frac{1}{2}\left(\frac{\partial v_x}{\partial r} + \frac{\partial v_r}{\partial x}\right) & \frac{\partial v_r}{\partial r} \end{pmatrix} : \begin{pmatrix} \frac{\partial \tilde{v}_x}{\partial x} & \frac{\partial \tilde{v}_x}{\partial r} \\ \frac{\partial \tilde{v}_r}{\partial x} & \frac{\partial \tilde{v}_r}{\partial r} \end{pmatrix} + 2\mu\frac{v_r}{r}\frac{\tilde{v}_r}{r}. \end{aligned} \tag{1.24}$$

The integrals over $\widetilde{\Omega}_1$ are simplified using the independence on φ coordinate

$$\int_{\widetilde{\Omega}_1} f(x,r)\,dx = \int_0^{2\pi}\int_{\Omega_1} r f(x,r)\,dx\,d\varphi = 2\pi\int_{\Omega_1} r f(x,r)\,dx. \tag{1.25}$$

Let us now consider the equation in the original two-dimensional cross section Ω_1 with Cartesian coordinates, we define the function $\mathbf{u} : (0,T)\times\Omega_1 \to \mathbb{R}^2$ as $\mathbf{u} = (u_1, u_2) = (v_x, v_r)$ and analogously $\tilde{\mathbf{u}} = (\tilde{v}_x, \tilde{v}_r)$. Using the fact that $\mathbf{u}$ is a function defied in Cartesian coordinates, we can rewrite (1.24) in the following form

$$\mathbb{T} : \nabla\tilde{\mathbf{v}} = -p\,\mathrm{div}\,\mathbf{u} - p\frac{\tilde{u}_2}{r} + 2\mu\mathbb{D}(\mathbf{u}) : \nabla\tilde{\mathbf{u}} + 2\mu\frac{u_2}{r}\frac{\tilde{u}_2}{r}.$$

The equations (1.23) and (1.21) are thus equivalent to the following

$$\int_{\Omega_1}\rho r\left(\frac{\partial\mathbf{u}}{\partial t} + V\frac{\partial\mathbf{u}}{\partial x}\right)\cdot\tilde{\mathbf{u}}\,dx + \int_{\Omega_1} r\mathbb{T}_{\mathbf{u}} : \nabla\tilde{\mathbf{u}}\,dx + \int_{\Omega_1}\left(-p + 2\mu\frac{u_2}{r}\right)\tilde{u}_2\,dx = 0, \tag{1.26}$$

$$\int_{\Omega_1}(r\mathrm{div}\,\mathbf{u} + u_2)\tilde{p}\,dx = 0, \tag{1.27}$$

where the Cauchy stress tensor $\mathbb{T}_{\mathbf{u}}$ is defined by the identity

$$\mathbb{T}_{\mathbf{u}} = -p(x,r)\mathbb{I} + 2\mu\mathbb{D}(\mathbf{u}).$$

To define the weak solution, we denote by $\mathbf{u}_b$ the boundary condition on $\Gamma_\mathrm{b}\cup\Gamma_1$ and define suitable function spaces

$$\mathbb{V} = \left\{\mathbf{u}\in W^{1,2}(\Omega_1,\mathbb{R}^2), \mathbf{u}\Big|_{\Gamma_\mathrm{b}} = \mathbf{u}_b, \mathbf{u}\Big|_{\Gamma_1} = \mathbf{u}_b, u_2\Big|_{\Gamma_0} = 0\right\},$$
$$\mathbb{V}_0 = \left\{\mathbf{u}\in W^{1,2}(\Omega_1,\mathbb{R}^2), \mathbf{u}\Big|_{\Gamma_\mathrm{b}} = \mathbf{0}, \mathbf{u}\Big|_{\Gamma_1} = \mathbf{0}, u_2\Big|_{\Gamma_0} = 0\right\}.$$

The functions $\mathbf{u}\in L^2(0,T;\mathbb{V})$ and $p\in L^2(0,T;L^2(\Omega_1))$ such that the time derivative $\frac{\partial\mathbf{u}}{\partial t}\in L^2(0,T;L^2(\Omega_1))$ are a weak solution if for every pair of test functions $\tilde{\mathbf{u}}\in\mathbb{V}_0$ and $\tilde{p}\in L^2(\Omega_1)$ and almost all $t\in(0,T)$ the equations (1.26) and (1.27) hold.

In the case of a steady flow, we prescribe the following boundary conditions

$$\begin{aligned} \mathbf{u} &= \mathbf{0} && \text{on } \Gamma_{\mathrm{b}}, \\ \mathbf{u} &= (V, 0) && \text{on } \Gamma_1, \\ u_2 &= 0 && \text{on } \Gamma_0. \end{aligned}$$

In the case in which the sphere moves through a stationary fluid the boundary conditions are

$$\begin{aligned} \mathbf{u} &= (-V, 0) && \text{on } \Gamma_{\mathrm{b}}, \\ \mathbf{u} &= \mathbf{0} && \text{on } \Gamma_1, \\ u_2 &= 0 && \text{on } \Gamma_0. \end{aligned}$$

In both cases, the drag force can be obtained from the velocity and pressure by integrating the traction over Γ_{b}. However, we must keep in mind that the total force acting on semicircle Γ_{b} is not directly the force acting on the sphere. We apply the correction for cylindrical coordinates in the integration

$$F_{\mathrm{D}} = \int_{\widetilde{\Gamma}_b} t_x \, dS = \int_0^{2\pi} \int_{\Gamma} r t_x(x, r) \, dl \, d\varphi = \int_{\Gamma_{\mathrm{b}}} 2\pi r \left(\mathbb{T}_{\mathbf{u}} \mathbf{n}\right)_x \, dl.$$

1.3.2 Space discretization

We discretize equation (1.26) and (1.27) in each time step (see below) using the finite element method. As a first step, we approximate the domain Ω_1 with a triangular mesh. Let us denote $\mathcal{T}_h$ the set of triangles in the mesh, in this case h represents the size of the triangles in triangulation. One may imagine h as the length of the longest edge or the diameter of circumscribed circle of the largest triangle in $\mathcal{T}_h$. While the precise interpretation is not important, we assume that lowering parameter h results in finer mesh. The fundamental requirements on $\mathcal{T}_h$ for our triangulation to make sense are:

1. The intersection of two distinct triangles from $\mathcal{T}_h$ is either empty set, common vertex or common edge.
2. No vertex lies outside $\overline{\Omega}_1$.
3. The domain Ω_1 is covered by $\mathcal{T}_h$, i.e. $\Omega_1 \subset \bigcup_{T \in \mathcal{T}_h} T$.

The first shall always hold. However, it may be impossible to cover some domains in such way, that both the second and the third requirements hold. We therefore construct the triangulation in a way, that the vertices of boundary triangle edges lie on $\partial\Omega_1$ as indicated in Figure 1.2. This approach fulfills the second requirement and for most domain shapes the domain Ω_1 is almost covered in the following sense

$$\left| \Omega_1 \setminus \bigcup_{T \in \mathcal{T}_h} T \right| \xrightarrow[h \to 0]{} 0.$$

To lower the computational complexity of the problem without significant loss of accuracy, we choose a non-uniform size of elements. The parts of Ω_1 closer to

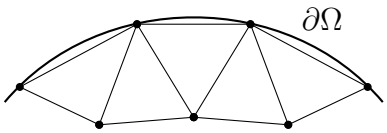

Figure 1.2: Approximation of domain boundary.

the particles are filled with finer mesh than parts of the domain that are further away. This approach is used throughout all numerical solutions presented in this thesis as the flow close to the particle surfaces is the most important and leaving distant elements larger introduces no significant error.

To generate the mesh, we start with simple mesh with uniform triangle size created by `mshr`, a mesh generating component of `FEniCS`. This mesh is then refined around the sphere surface Γ_b (a semicircle in this case) via triangle subdivisions to obtain finer mesh in some defined distance from Γ_b. The subdivision can be then repeated in gradually smaller distances from Γ_b as seen in Figure 1.3. It is important to move any nodes, that would appear outside the Ω_1 after subdivision of an outer boundary edge, back on the boundary $\partial\Omega_1$.

From this mesh, we want to go one step further and generate the triangular elements to have size proportional to square distance from the closest particle (or similar metric that may be easier to compute for specific particle shapes), with offset, coefficient and maximal value as variable parameters. In the case of circular particles, we have

$$\text{size} \approx \min\left(a\left(||\mathbf{x}-\mathbf{X}||^2 - R^2\right) + b, c\right), \tag{1.28}$$

where $\mathbf{X}$ and R are the center and the radius of the particle, for which this expression has the smallest value. For circles with identical radii, $\mathbf{X}$ and R are the center and the radius of the closest particle. This mesh is created from the mesh created using triangle subdivision, the specific method is described in the following chapter.

To approximate the solution, we use the Taylor-Hood elements. In other words, Lagrange elements of order two for the velocity field and Lagrange elements of order one for the pressure. A two-dimensional Lagrange finite element of order $k \in \{1, 2\}$ is a triplet (T, P_k, Σ_k), where T is a triangular closed set with vertices a_1, a_2, a_3, P_k is a space of polynomials of degree less than or equal to k on T, and Σ_k is a set of evaluation functionals in the vertices and the midpoints of edges

$$\Sigma_1 = \{\Phi_i; \forall p \in P_k : \Phi_i(p) = p(a_i); i = 1, 2, 3\},$$
$$\Sigma_2 = \Sigma_1 \cup \left\{\Phi_{ij}; \forall p \in P_k : \Phi_{ij}(p) = p\left(\frac{a_i + a_j}{2}\right); i, j = 1, 2, 3; i < j\right\}.$$

The functionals from Σ_k are called degrees of freedom and are represented by nodes in Figure 1.4. The Taylor-Hood elements are well suited for this problem as they satisfy the Ladyzhenskaya–Babuška–Brezzi (LBB) condition as proven by Verfürth [1984].

1.3.3 Time discretization

We finally see a significant difference between the two approaches. In the case of stationary flow, we assume the solution is independent of time, thus the time

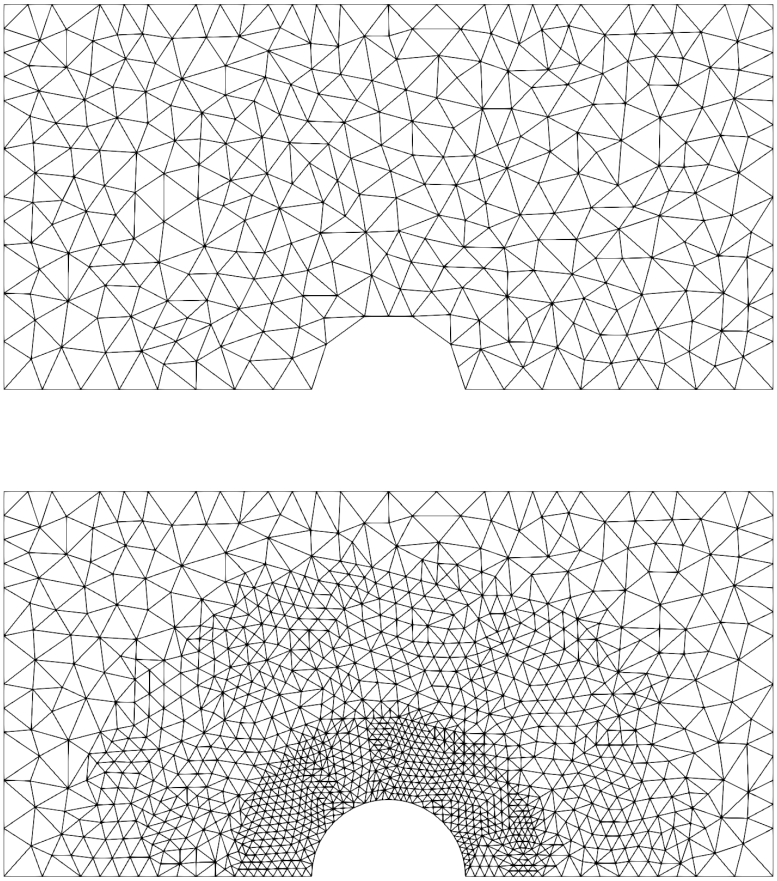

Figure 1.3: The original mesh (top) and the mesh after two iterations of subdivision refinement (bottom). The semicircle in the bottom represents a particle surface. Choosing finer mesh around the curved boundaries leads to much better approximation of such boundaries, while the number of triangles stays much lower than if the whole mesh was refined.

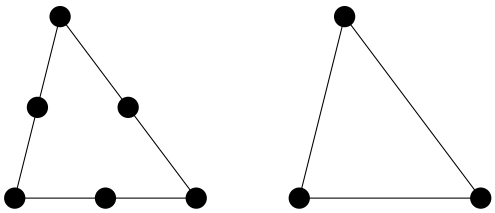

Figure 1.4: Lagrange element of the second order (left) with 6 degrees of freedom are used to approximate the velocity field using locally quadratic polynomials. Lagrange element of the first order (right) with 3 degrees of freedom are used to approximate the pressure field with locally linear polynomials. The polynomial function on the element is uniquely determined by values in nodes (degrees of freedom).

derivative vanishes and no time discretization is needed. In the second case, where the boundary moves, the situation is significantly more complicated. We want to find a time-dependent solution in domain $\Omega_1(t)$, with the domain itself

also evolving in time. More specifically, in each step, the boundary Γ_b moves by the vector $(-\Delta t\, V, 0)$, where Δt is the time step of discretization in time. Boundary Γ_0 then moves in the direction of x according to the shift of Ω_b such that the endpoints shared with Γ_1 stay fixed. For time discretization we use the backwards Euler discretization scheme. More specifically, in time $t = t_n$, where $t_n = t_0 + n\Delta t$, $n \in \mathbb{N}$, is the n-th time step, we approximate the time derivative with

$$\frac{\partial \mathbf{u}}{\partial t}(t_n, \mathbf{x}) \approx \frac{\mathbf{u}(t_n, \mathbf{x}) - \mathbf{u}(t_{n-1}, \mathbf{x})}{\Delta t}.$$

1.3.4 ALE Method

To capture the movement of the computational domain, we use the ALE (arbitrary Lagrangian-Eulerian) method described by Hughes et al. [1981]. The method is based on splitting the deformation into two parts as indicated in Figure 1.5, in our case it is the the fluid flow (described by the fluid velocity $\mathbf{u}$) and the movement of the domain (described by the mesh velocity $\mathbf{u}_\mathrm{mesh}$). By changing our approach from purely Eulerian description, we may expect some changes in governing equations. However, the only change that has to be made due to the ALE method is the introduction of the mesh velocity into the convection term of Navier-Stokes equations as described in Donea et al. [2004]

$$(\mathbf{u} \cdot \nabla)\, \mathbf{u} \quad \rightarrow \quad ((\mathbf{u} - \mathbf{u}_\mathrm{mesh}) \cdot \nabla)\, \mathbf{u}.$$

In the case of Oseen equations, we approximate this term by

$$((\mathbf{u} - \mathbf{u}_\mathrm{mesh}) \cdot \nabla)\, \mathbf{u} \approx ((\mathbf{V} - \mathbf{u}_\mathrm{mesh}) \cdot \nabla)\, \mathbf{u}.$$

This will also cause a slight change in the weak formulation, the first term in equation (1.26) is replaced by

$$\int_{\Omega_1} \rho r \left(\frac{\partial \mathbf{u}}{\partial t} + \nabla \mathbf{u}(\mathbf{V} - \mathbf{u}_\mathrm{mesh}) \right) \cdot \tilde{\mathbf{u}}\, dx. \tag{1.29}$$

In practice for problems in this chapter, the mesh movement function $\mathbf{u}_\mathrm{mesh}$ is chosen as a harmonic function satisfying the boundary conditions for $\mathbf{u}$. The movement of the mesh is implemented using `ALE.move()` function in the `FEniCS` library, which moves all nodes in the computational mesh according to a prescribed vector field.

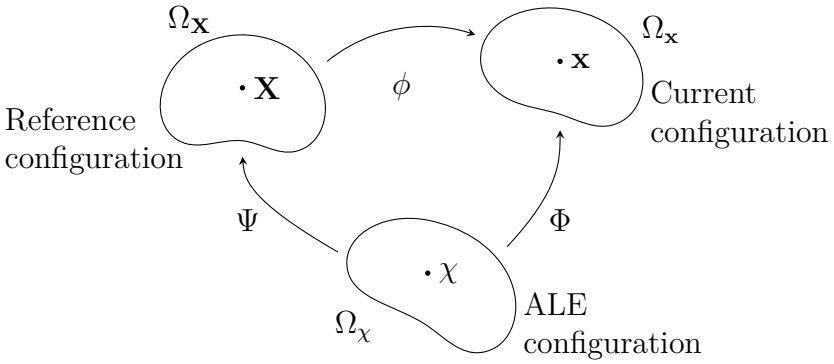

Figure 1.5: The diagram used by Donea et al. [2004]. The domain $\Omega_{\mathbf{x}}$ represents the current configuration and $\Omega_{\mathbf{X}}$ represents the reference material configuration. Instead of defining the problem on $\Omega_{\mathbf{x}}$ or $\Omega_{\mathbf{X}}$, we instead formulate the problem on the ALE domain Ω_{χ}, where Φ is the movement of the mesh. Clearly the choice $\Phi = \mathbf{I}$ results in Eulerian description, whereas $\Psi = \mathbf{I}$ results in Lagrangian description.

1.4 Numerical results

As seen in Figure 1.6, both methods approximate closely the linear relation of Stokes formula. One may notice that the ALE method deviates slightly from Stokes law for higher velocities. There are more effects that may cause this, we shall investigate the effect of some parameters.

As stated above, the Stokes formula assumes $\mathrm{Re} \ll 1$, we can therefore expect the drag in numerical approximation to be closer to Stokes formula for smaller values of Reynold number. We explore this effect by investigating the role of viscosity. The results can be seen in Figure 1.7. We can clearly see that the force does not depend linearly on the sphere velocity for $\mu = 0.1\,\mathrm{Pa}\cdot\mathrm{s}$, where the Reynolds numbers is up to $\mathrm{Re} = 2$. Both methods get closer to the Stokes formula with increasing viscosity (and in turn decreasing Reynolds number). However, the solution using ALE method seem to be more sensitive to this effect, in this case the flow at $t = 1\,\mathrm{s}$ might not have converged to the stationary solution yet.

Convergence in time of the numerical solution using ALE method is given in Figure 1.8. We can observe that the drag force converges to a stationary value faster in the case with higher viscosity. Measuring the drag force later might give more accurate result for $\mu = 10\,\mathrm{Pa}\cdot\mathrm{s}$, but we would also see little improvement in case $\mu = 100\,\mathrm{Pa}\cdot\mathrm{s}$. Some minor improvement in Stokes formula approximation can be achieved by choosing smaller time step, which can be seen clearly in Figure 1.8.

The last significant factor that we study is the size of the domain. As seen in Figure 1.9, the domain has to be large enough to approximate well the infinite domain assumed in the derivation of the Stokes formula. As one would predict, for smaller sizes the boundary condition prescribed on Γ_1 influences the flow close to sphere surface more than if the same velocity would be prescribed further away. The effect is almost identical in stationary flow calculation, it is not ALE specific.

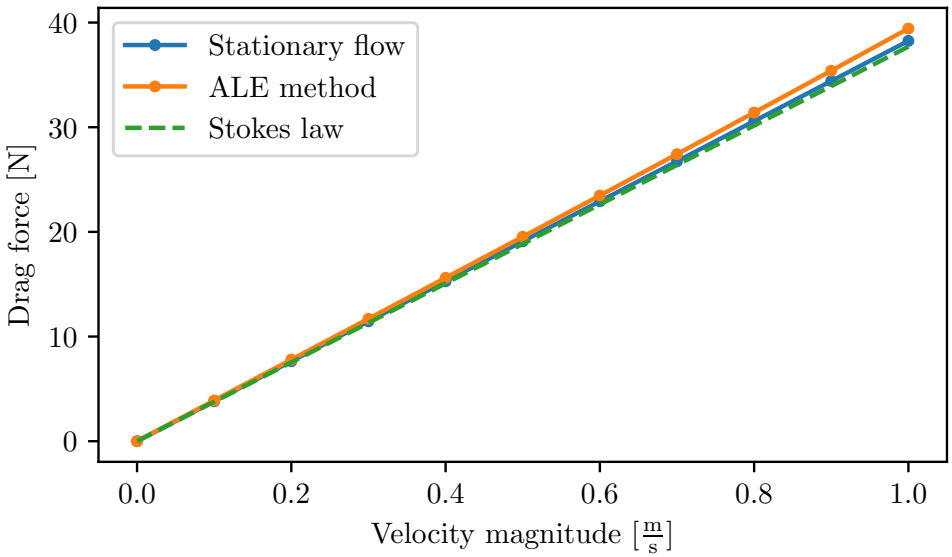

Figure 1.6: The dependence of the drag force (y axis) on the magnitude of velocity (x axis). The viscosity of the fluid is chosen to be $\mu = 10\,\mathrm{Pa}\cdot\mathrm{s}$ and density $\rho = 1\,\frac{\mathrm{kg}}{\mathrm{m}^3}$, the size of computational domain is 60 m (width) by 40 m (height) and the radius of the sphere is $R = 0.2\,\mathrm{m}$. The center of the sphere (represented by a semicircle) is located at distance 20 m from the left border for the stationary case. In ALE case, the sphere center is in the middle of lower border and moves towards the left border. We used the time step $\Delta t = 0.1\,\mathrm{s}$ in ALE case, the force is calculated at time $t = 1\,\mathrm{s}$.

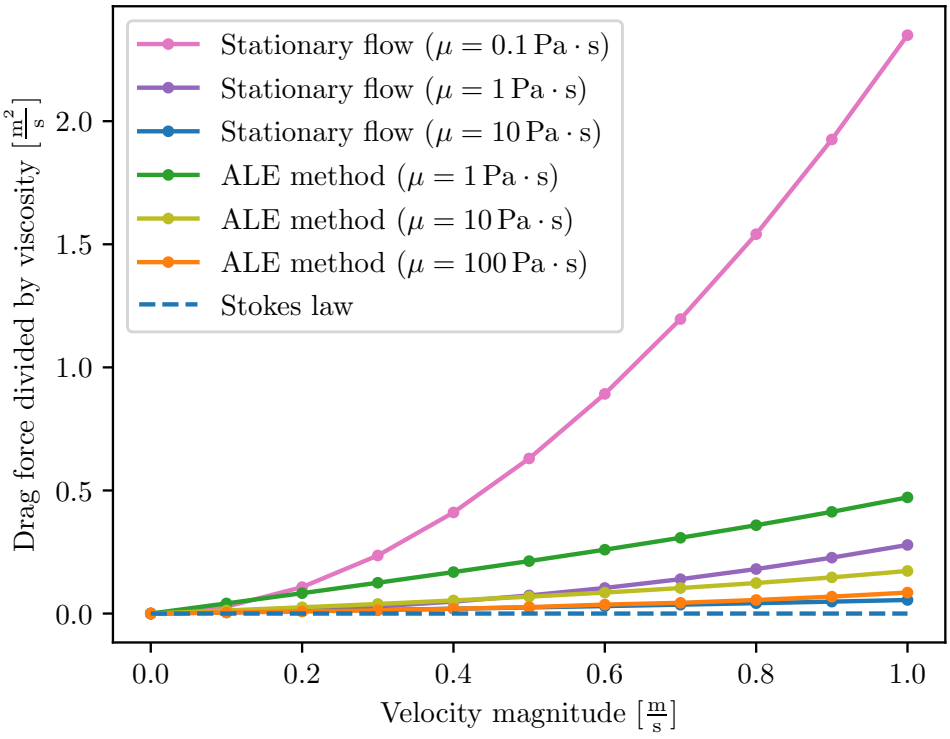

Figure 1.7: The dependence of the difference between the drag measured in the numerical simulation and the drag predicted by Stokes formula (y axis) on the magnitude of velocity $\mathbf{V}$ (x axis) for various viscosities. All parameters except the viscosity are the same as described in the caption of the Figure 1.6. As the force in Stokes formula is proportional to viscosity, we divide all results by viscosity to enable the comparison.

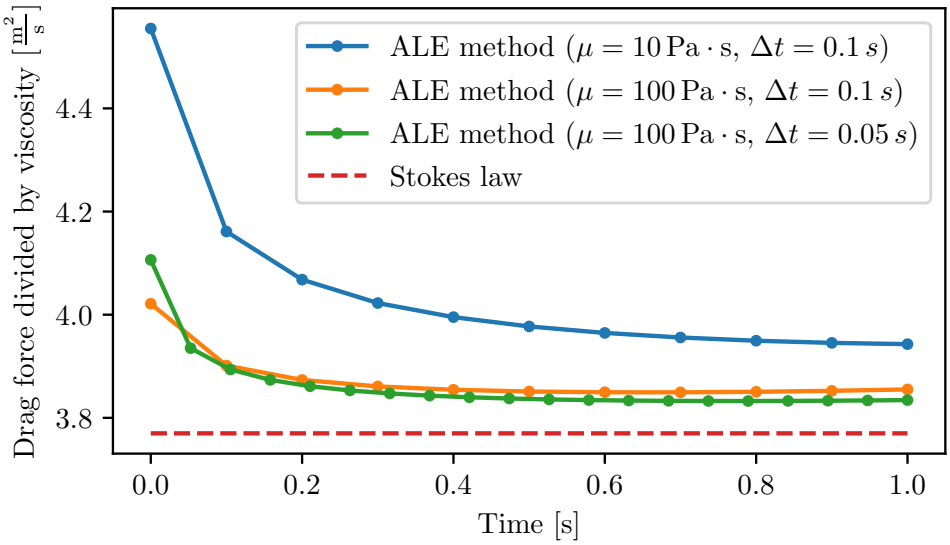

Figure 1.8: The dependence of the drag force acting on sphere surface in ALE method divided by viscosity (y axis) on time (x axis). All parameters are the same as described in the caption of the Figure 1.6, but the velocity magnitude is set to a fixed value $V = 1\,\frac{\mathrm{m}}{\mathrm{s}}$. A numerical solution with time step $\Delta t = 0.05\,\mathrm{s}$ is added for comparison.

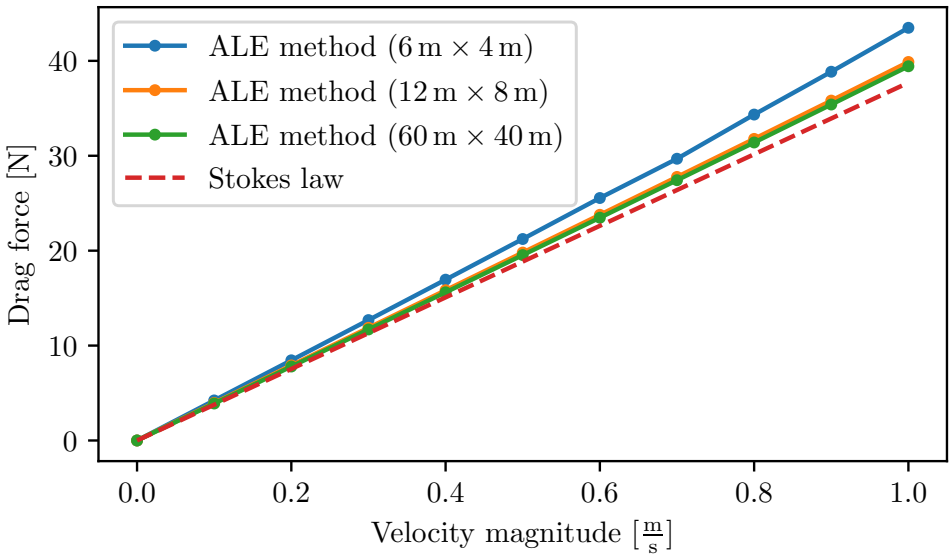

Figure 1.9: The dependence of the drag force acting on sphere surface in ALE method (y axis) on the velocity magnitude (x axis) computed in domains of different sizes. All parameters, apart from the domain size, are the same as described in the caption of the Figure 1.6. In particular, no parameters, with the only exception being the domain size, change across the computations with different domain sizes. Initially, the ball center lies in the middle of the lower border.

2. Two-way coupled method description

In this chapter we move from simple model shown in the previous chapter, where particle velocity was prescribed, to a model where the particle velocity and the angular velocity are determined by the fluid flow. We derive the numerical model presented in Hu et al. [2001]. This model includes the required two-way coupling between particle movement and fluid flow. Furthermore, this approach can be implemented with finite element method in Python using `FEniCS` library. We present details of our implementation in this chapter, the results obtained using this method can be found in the following chapters.

2.1 Derivation of weak formulation

In this section we describe the derivation of the weak formulation of the problem that models a flow of fluid with N submerged rigid particles. The method is derived in two dimensions, as we aim to compute the numerical simulation for the two-dimensional case only. However, the derivation of fully three-dimensional model would differ only in the description of particle rotation, as we would need a vector to describe particles rotation instead of a scalar.

Let $\Omega_0(t)$ denote the domain occupied by the fluid at the time $t \in [0, T]$. Then for the i-th particle, we denote the domain occupied by the particle by $\Omega_i(t)$, where $i = 1, ..., N$. We assume that $\Omega_0(t), \Omega_1(t), ..., \Omega_N(t)$ are disjoint for every time t and we further assume that the boundary $\partial\Omega_0(t)$ consists of $N+1$ connected disjoint subsets, more precisely, it can be represented as

$$\partial\Omega_0(t) = \left(\bigcup_{i=1}^{N} \partial\Omega_i(t)\right) \cup \Gamma_0,$$

where Γ_0 denotes the fixed part of the boundary (in most cases the outer boundary of the domain $\Omega_0(t)$). The example of such configuration is shown in Figure 2.1.

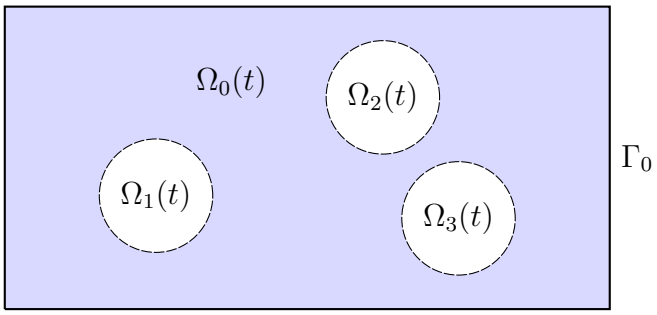

Figure 2.1: Domain $\Omega_0(t)$ is occupied by the fluid at time t, in this domain three particles are cut out. The particles Ω_i, $i = 1, 2, 3$, move in a rigid motion through the fluid. The outer boundary Γ_0 is considered to be fixed.

We prescribe the homogeneous incompressible Navier-Stokes equations inside the domain $\Omega_0(t)$. Let us denote $Q = \{(t, \mathbf{x}), \mathbf{x} \in \Omega_0(t)\}$. We are looking for

a velocity function $\mathbf{v} : Q \to \mathbb{R}^2$ and a pressure function $p : Q \to \mathbb{R}$ fulfilling the following equations in Q

$$\operatorname{div} \mathbf{v} = 0, \tag{2.1}$$

$$\rho \left(\frac{\partial \mathbf{v}}{\partial t} + (\mathbf{v} \cdot \nabla)\mathbf{v} \right) = \operatorname{div} \mathbb{T} + \rho \mathbf{f}, \tag{2.2}$$

$$T = -p\mathbb{I} + \mu \left(\nabla \mathbf{v} + (\nabla \mathbf{v})^T \right), \tag{2.3}$$

where μ is the dynamic shear viscosity, ρ is the density of the fluid and $\mathbf{f}$ is the external acceleration, such as gravity. We prescribe the no-slip boundary condition on $\partial\Omega_0(t)$. However, we need the velocity on the surface of the i-th particle to be zero *with respect to the movement of the corresponding particle*, we thus have to define the velocity and the angular velocity for each particle. These quantities are for i-th particle denoted by $\mathbf{V}_i$ and ω_i respectively. Accounting for the velocity and angular velocity of the i-th particle, we prescribe the following boundary conditions

$$\mathbf{v}(t, \mathbf{x}) = \mathbf{v}_0(t, \mathbf{x}) \qquad \text{on } \Gamma_0, \tag{2.4}$$

$$\mathbf{v}(t, \mathbf{x}) = \mathbf{V}_i(t) + \omega_i(t) \times (\mathbf{x} - \mathbf{X}_i(t)) \qquad \text{on } \partial\Omega_i(t), \tag{2.5}$$

where $\mathbf{v}_0 : [0, T] \times \Gamma \to \mathbb{R}^2$ is the prescribed boundary condition and $a \times \mathbf{b}$ for arbitrary $a \in \mathbb{R}$ and $\mathbf{b} \in \mathbb{R}^2$ is defined as

$$a \times \mathbf{b} = \begin{pmatrix} -ab_2 \\ ab_1 \end{pmatrix} = \begin{pmatrix} 0 \\ 0 \\ a \end{pmatrix} \times \begin{pmatrix} b_1 \\ b_2 \\ 0 \end{pmatrix} \Bigg|_{\mathbb{R}^2}.$$

In this derivation, we assume that the Dirichlet boundary condition is prescribed on the outer boundary, but any different boundary condition may be prescribed on Γ_0 without any additional difficulty.

The forces acting on the i-th particle with mass m_i can be split into an external force $\mathbf{F}_i$ and the force caused by interaction with fluid, which is computed by integrating the traction as defined by (1.19) over the particle boundary. From the second Newton law, we therefore obtain the equation for particle velocity

$$\frac{d(m_i \mathbf{V}_i)}{dt} = \mathbf{F}_i - \int_{\partial\Omega_i(t)} \mathbb{T}\mathbf{n}(x)\, dS, \tag{2.6}$$

where $\mathbf{n}$ is the outer unit normal to $\partial\Omega_i(t)$, which is in the opposite direction to the outer unit normal of $\partial\Omega_0(t)$, this results in the negative sign in front of the surface integral. Analogously, we obtain the total torque acting on particle from the traction, the second impulse law states

$$\frac{d}{dt}(I_i \omega_i) = -\int_{\partial\Omega_i(t)} (\mathbf{x} - \mathbf{X}_i) \times \mathbb{T}\mathbf{n}\, dS, \tag{2.7}$$

where I_i is the tensor of inertia, which is in the two-dimensional case reduced to a scalar value. After the particle velocity and angular velocity are obtained, the position $\mathbf{X}_i$ and rotation θ_i of the i-th particle can be simply computed as a solution of following equations

$$\begin{aligned} \frac{d\mathbf{X}_i}{dt} &= \mathbf{V}_i, \\ \frac{d\theta_i}{dt} &= \omega_i. \end{aligned} \tag{2.8}$$

The initial conditions for differential equations (2.8) are the initial particle position and rotation respectively.

As a next step we derive the form of the weak formulation of this problem at a fixed time step t. Let us now choose an arbitrary test functions $\tilde{\mathbf{v}} \in C^2(\Omega_0(t), \mathbb{R}^2)$, $\tilde{V}_i \in \mathbb{R}^2$ and $\tilde{\omega}_i \in \mathbb{R}$, $i = 1, \ldots, N$, which fulfill the boundary conditions (2.4) and (2.5) with $v_0 = 0$. We now multiply equation (2.2) by $\tilde{\mathbf{v}}$ and integrate over the domain $\Omega_0(t)$

$$\int_{\Omega_0(t)} \rho \left(\frac{\partial \mathbf{v}}{\partial t} + (\mathbf{v} \cdot \nabla)\mathbf{v} - \mathbf{f} \right) \cdot \tilde{\mathbf{v}} \, dx - \int_{\Omega_0(t)} \operatorname{div}(\mathbb{T})\tilde{\mathbf{v}} \, dx = 0. \tag{2.9}$$

To simplify the notation, we define the material derivative as

$$\frac{d\mathbf{v}}{dt} = \frac{\partial \mathbf{v}}{\partial t} + (\mathbf{v} \cdot \nabla)\mathbf{v}.$$

Using the properties of $\partial\Omega_0(t)$, symmetry of $\mathbb{T}$ and the Gauss divergence theorem, with the assumption that the solution and the domain have sufficient regularity, we obtain the following equality

$$-\int_{\Omega_0(t)} (\operatorname{div} \mathbb{T})\tilde{\mathbf{v}} \, dx = \int_{\Omega_0(t)} \mathbb{T} : \nabla \tilde{\mathbf{v}} \, dx - \sum_{i=1}^{N} \int_{\partial\Omega_i(t)} (\mathbb{T}\mathbf{n}) \cdot \tilde{\mathbf{v}} \, dS. \tag{2.10}$$

Substituting this identity into (2.9) results in the following equation

$$\int_{\Omega_0(t)} \rho \left(\frac{d\mathbf{v}}{dt} - \mathbf{f} \right) \cdot \tilde{\mathbf{v}} \, dx + \int_{\Omega_0(t)} \mathbb{T} : \nabla \tilde{v} \, dx - \sum_{i=1}^{N} \int_{\partial\Omega_i(t)} (\mathbb{T}\mathbf{n}) \cdot \tilde{\mathbf{v}} \, dS = 0. \tag{2.11}$$

Using the notation $\tilde{\mathbf{v}}_\mathrm{b} = \tilde{\mathbf{V}}_i + \tilde{\omega}_i \times (\mathbf{x} - \mathbf{X}_i)$, the integral over particle boundary is expanded to a form

$$-\int_{\partial\Omega_i(t)} (\mathbb{T}\mathbf{n}) \cdot \tilde{\mathbf{v}} \, dS = -\int_{\partial\Omega_i(t)} (\mathbb{T}\mathbf{n}) \cdot (\tilde{\mathbf{v}}_\mathrm{b}) \, dS - \int_{\partial\Omega_i(t)} (\mathbb{T}\mathbf{n}) \cdot (\tilde{\mathbf{v}} - \tilde{\mathbf{v}}_\mathrm{b}) \, dS. \tag{2.12}$$

The second term is omitted with the assumption that $\tilde{\mathbf{v}}$ satisfies (2.5). Using equations (2.6) and (2.7), we further simplify (2.12) to the following form

$$\begin{aligned} -\int_{\partial\Omega_i(t)} (\mathbb{T}\mathbf{n}) \cdot \tilde{\mathbf{v}}_\mathrm{b} \, dS &= -\int_{\partial\Omega_i(t)} (\mathbb{T}\mathbf{n}) \cdot (\tilde{\mathbf{V}}_i + \tilde{\omega}_i \times (\mathbf{x} - \mathbf{X}_i)) \, dS \\ &= \tilde{\mathbf{V}}_i \cdot \left(\frac{d(m_i \mathbf{V}_i)}{dt} - \mathbf{F}_i \right) - \tilde{\omega}_i \int_{\partial\Omega_i(t)} (\mathbf{x} - \mathbf{X}_i) \times (\mathbb{T}\mathbf{n}) \, dS \\ &= \tilde{\mathbf{V}}_i \cdot \left(\frac{d(m_i \mathbf{V}_i)}{dt} - \mathbf{F}_i \right) + \tilde{\omega}_i \frac{d(I_i \omega_i)}{dt} \end{aligned}$$

By substituting this result into (2.11), we obtain the following equation

$$\int_{\Omega_0(t)} \rho \left(\frac{d\mathbf{v}}{dt} - \mathbf{f} \right) \cdot \tilde{\mathbf{v}} + \mathbb{T} : \nabla \tilde{v} \, dx + \sum_{i=1}^{N} \tilde{\mathbf{V}}_i \cdot \left(\frac{d(m_i \mathbf{V}_i)}{dt} - \mathbf{F}_i \right) + \sum_{i=1}^{N} \tilde{\omega}_i \frac{d(I_i \omega_i)}{dt} = 0. \tag{2.13}$$

To get the weak formulation of the continuity equation, we multiply the continuity equation (2.1) by an arbitrary test function $\tilde{p} \in C(\Omega_0(t))$ and integrate over the domain $\Omega_0(t)$ to obtain

$$\int_{\Omega_0(t)} \tilde{p} \operatorname{div} \mathbf{v} \, dx = 0. \tag{2.14}$$

To define a weak solution, we first employ the time discretization. We split the time interval into discrete nodes t_n, $n \in \{0, 1, \ldots, N\}$, in such a way, that $t_n = t_{n-1} + \Delta t$, where Δt is a fixed time step. The approximate solution at time step t_n is denoted by $\mathbf{v}^{(n)}$, $\mathbf{V}_i^{(n)}$, $\omega_i^{(n)}$ and $p^{(n)}$, analogously, the approximation of domain $\Omega_0(t_n)$ is denoted by $\Omega_0^{(n)}$. We employ the implicit Euler scheme, i.e. the discretized equation is formulated at time t_n and the time derivative is substituted with a backward difference

$$\begin{aligned}
\frac{\partial \mathbf{v}}{\partial t}(t_n, \mathbf{x}) &\approx \frac{\mathbf{v}^{(n)}(\mathbf{x}) - \mathbf{v}^{(n-1)}(\Phi^{-1}(\mathbf{x}))}{\Delta t}, \\
\frac{\partial \mathbf{V}_i}{\partial t}(t_n) &\approx \frac{\mathbf{V}_i^{(n)} - \mathbf{V}_i^{(n-1)}}{\Delta t}, \\
\frac{\partial \omega_i}{\partial t}(t_n) &\approx \frac{\omega_i^{(n)} - \omega_i^{(n-1)}}{\Delta t},
\end{aligned} \tag{2.15}$$

where Φ is the mapping from $\Omega_0^{(n-1)}$ to $\Omega_0^{(n)}$ that is equivalent to the movement of the mesh and implemented with `ALE.move()`.

Let us now define the function spaces for the weak solution at time t_n. The space for the solution is defined as follows

$$\begin{aligned}
\mathbb{V}^{(n)} = \Big\{ &(\mathbf{v}, \mathbf{V}_1, \ldots, \mathbf{V}_N, \omega_1, \ldots, \omega_N); \mathbf{v} \in W^{1,2}(\Omega_0^{(n)}); \mathbf{v} = \mathbf{v}_0 \text{ on } \Gamma_0; \\
&\mathbf{v} = \mathbf{V}_i + \omega_i \times (\mathbf{x} - \mathbf{X}_i) \text{ on } \partial\Omega_i^{(n)}, \mathbf{V}_i \in \mathbb{R}, \omega_i \in \mathbb{R}, i = 1, \ldots, N \Big\}.
\end{aligned} \tag{2.16}$$

The space $\mathbb{V}_0^{(n)}$ for the test functions is defined in the same way, but the boundary condition on Γ_0 is replaced with $\mathbf{v} = \mathbf{0}$. For the pressure function, we define the space

$$\mathbb{Q}^{(n)} = \left\{ p \in L^2(\Omega_0^{(n)}), \int_{\Omega_0^{(n)}} p \, dx = 0 \right\}.$$

The pressure p is present in equation only tn the form ∇p, the solution for a Dirichlet boundary condition on Γ_0 is therefore not determined uniquely without the additional condition $\int_{\Omega_0^{(n)}} p \, dx = 0$. In the numerical implementation, this can be replaced with condition $p(\mathbf{x}_0) = 0$, where $\mathbf{x}_0 \in \bar{\Omega}_0$ is an arbitrarily chosen fixed point. We further assume that the initial condition $\mathbf{U}^{(0)} \in \mathbb{V}^{(0)}$ is provided.

A pair $\mathbf{U}^{(n)} \in \mathbb{V}^{(n)}$ and $p^{(n)} \in \mathbb{Q}^{(n)}$, where

$$\mathbf{U}^{(n)} = (\mathbf{v}^{(n)}, \mathbf{V}_1^{(n)}, \ldots, \mathbf{V}_N^{(n)}, \omega_1^{(n)}, \ldots, \omega_N^{(n)}),$$

is a weak solution of the system described by equation (2.1)-(2.8) at time $t = t_n$ if the identities (2.13) and (2.14) with approximation (2.15) hold for all $\tilde{\mathbf{U}} \in \mathbb{V}^{(n)}$ and $p \in L^2(\Omega_0(t))$, where

$$\tilde{\mathbf{U}} = (\tilde{\mathbf{v}}, \tilde{\mathbf{V}}_1, \ldots, \tilde{\mathbf{V}}_N, \tilde{\omega}_1, \ldots, \tilde{\omega}_N).$$

2.2 Numerical implementation

The space discretization is done in the same way as described in Subsection 1.3.2. Namely, the Taylor-Hood hood finite elements are used. The previously described

mesh generation is also used as a starting point to go one step further and generate the triangular elements to have size proportional to square distance from the closest particle (or similar metric that may be easier to compute for specific particle shapes), with offset, coefficient and maximal value as variable parameters. In the case of circular particles, we use

$$\text{size} \approx \min\left(a\left(||\mathbf{x}-\mathbf{X}||^2 - R^2\right) + b, c\right), \tag{2.17}$$

where $\mathbf{X}$ and R are the center and the radius of the particle, for which this expression has the smallest value. For circles with identical radii, $\mathbf{X}$ and R are the center and the radius of the closest particle.

2.2.1 Boundary condition

As described above, we have a system of equations for functions $\mathbf{v}$, p, $\mathbf{V}_i$ and ω_i, for $i = 1, \ldots, N$. Only $\mathbf{v}$ and p are obtained using conventional finite element method, by approximating the solution with locally polynomial functions. For velocities $\mathbf{V}_i$ and angular velocities ω_i, we have the ordinary differential equations approximated using finite differences, that describe the change of these values in time. However, these two pairs of function are not independent as they are linked via the boundary conditions imposed on velocity $\mathbf{v}$. This makes the problem rather difficult, as in `FEniCS` it is not directly possible to prescribe a boundary conditions, that contain unknown variables. We therefore need to add another term to equation (2.13) to enforce this boundary condition. The simple solution to this would be a basic penalization method

$$C\int_{\partial\Omega_i} (\mathbf{v} - (\mathbf{V}_i + \omega_i \times (\mathbf{x} - \mathbf{X}_i))) \cdot \left(\tilde{\mathbf{v}} - (\tilde{\mathbf{V}}_i + \tilde{\omega}_i \times (\mathbf{x} - \mathbf{X}_i))\right) \, dS.$$

The disadvantage of this approach is the size of the constant C, which has to be very large to obtain reasonable solution, and may therefore cause some numerical complication.

Instead of the straightforward approach, we use the symmetric Nitsche method described by Nitsche [1971]. Let us for simplicity denote

$$\begin{aligned}\mathbf{v}_b(\mathbf{V}_i, \omega_i) &= \mathbf{V}_i + \tilde{\omega}_i \times (\mathbf{x} - \mathbf{X}_i),\\ \mathbb{T}(\mathbf{v}, p) &= -p\mathbb{I} + \mu\left(\nabla\mathbf{v} + (\nabla\mathbf{v})^T\right).\end{aligned}$$

In this case, we keep the last term in (2.12) as a part of the equation. On top of that, we multiply the difference $\mathbf{v} - \mathbf{v}_b(\mathbf{V}_i, \omega_i)$ by a test function $\tilde{\Phi} \in L^2(\partial\Omega)$ and integrate over $\partial\Omega_i$

$$\int_{\partial\Omega_i} \tilde{\Phi} \cdot (\mathbf{v} - \mathbf{v}_b(\mathbf{V}_i, \omega_i)) \, dS.$$

As the velocity $\mathbf{v}$ is equal to $\mathbf{v}_b(\mathbf{V}_i, \omega_i)$ due to the boundary condition (2.5), this integral is equal to zero for any test function. Using a specific choice of the test function $\tilde{\Phi}$, we obtain

$$\int_{\partial\Omega_i} \mathbb{T}(\tilde{\mathbf{v}}, \tilde{p})\mathbf{n} \cdot (\mathbf{v} - \mathbf{v}_b(\mathbf{V}_i, \omega_i)) \, dS.$$

As described in Chabiniok et al. [2021], the formulation is stable if the following stabilization term is added

$$\int_{\partial\Omega_i} 2\frac{\beta}{h}\left(\mathbf{v} - \mathbf{v}_b(\mathbf{V}_i, \omega_i)\right) \cdot \tilde{\mathbf{v}}\, dS,$$

with sufficiently large parameter $\beta > 0$. In this case, h denotes a local size of mesh edge. The whole term added to equation (2.13) is then the following

$$\begin{aligned} F_{\text{Nitsche}} = -\sum_{i=1}^{N} \int_{\partial\Omega_i} & \mathbb{T}(\mathbf{v}, p)\mathbf{n} \cdot (\tilde{\mathbf{v}} - \mathbf{v}_b(\tilde{\mathbf{V}}_i, \tilde{\omega}_i)) \\ & + \mathbb{T}(\tilde{\mathbf{v}}, \tilde{p})\mathbf{n} \cdot (\mathbf{v} - \mathbf{v}_b(\mathbf{V}_i, \omega_i)) \\ & - 2\frac{\beta}{h}\left(\mathbf{v} - \mathbf{v}_b(\mathbf{V}_i, \omega_i)\right) \cdot \tilde{\mathbf{v}}\, dS. \end{aligned}$$

The parameter $\frac{\beta}{h}$ is usually chosen between 10 and 10^4, but the solution does not depend on the precise choice of this parameter.

2.2.2 Mesh movement

To describe the movement of our mesh, we use the ALE method as described in the previous chapter. This approach results in the introduction of the mesh velocity $\mathbf{v}_{\text{mesh}}$ in the convective term of the balance of linear momentum

$$(\mathbf{v} \cdot \nabla)\,\mathbf{v} \quad \rightarrow \quad ((\mathbf{v} - \mathbf{v}_{\text{mesh}}) \cdot \nabla)\,\mathbf{v}.$$

Mesh velocity $\mathbf{v}_{\text{mesh}}$ should be a function that is zero on the outer boundary and equal to particle velocity on particle surface. For circular particles, we define this function as a solution of the following equation

$$\begin{aligned} \Delta\mathbf{v}_{\text{mesh}} &= 0, \\ \mathbf{v}_{\text{mesh}} &= \mathbf{V}_i \quad \text{on } \partial\Omega_i(t), \\ \mathbf{v}_{\text{mesh}} &= 0 \quad \text{on } \partial\Omega_0(t). \end{aligned} \tag{2.18}$$

This approach results in a smooth mesh velocity function that can be easily obtained numerically. In the case of non-circular particles, the movement on particle boundary is more complicated as we have to account for the particle rotation. To solve this problem, one may prescribe the same boundary condition used for the fluid velocity $\mathbf{V}_i + \omega_i \times (\mathbf{x} - \mathbf{X}_i)$. However, let us imagine a rotating circle without any sliding motion. Each node on the boundary of this circle moves on a straight line in the direction of local tangent vector each time step. The distance from the center necessarily rises, which clearly leads to an expansion of this circle in each step. We clearly need a better approach.

Let us divide the particle motion in two parts, the sliding motion and the rotational motion. Let us denote the position vector of a boundary point $\mathbf{x}$ relative to particle center by $\mathbf{r} = \mathbf{x} - \mathbf{X}_i$. To calculate the position of this point in the following step, we move the center by vector $\Delta t\, \mathbf{V}_i$ to get the center in the new step, and then add the vector $\mathbf{r}$ rotated by $\Delta t\, \omega_i$ to the new center as shown in Figure 2.2. The correct boundary condition is then

$$\mathbf{v}_{\text{mesh}} = \mathbf{V}_i + \frac{1}{\Delta t}\begin{pmatrix} \cos(\Delta t\, \omega_i) - 1 & -\sin(\Delta t\, \omega_i) \\ \sin(\Delta t\, \omega_i) & \cos(\Delta t\, \omega_i) - 1 \end{pmatrix} (\mathbf{x} - \mathbf{X}_i) \quad \text{on } \partial\Omega_i(t). \tag{2.19}$$

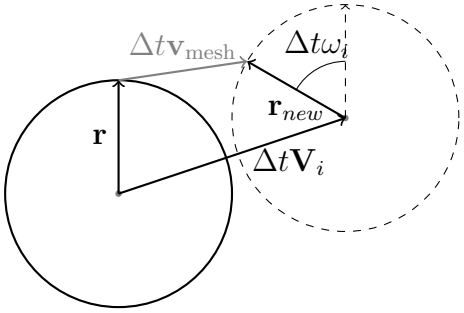

Figure 2.2: Movement of a particle divided into a sliding motion and rotational motion.

In some cases, the choice of a mesh velocity as a solution of (2.18) may cause the mesh movement to be concentrated in a proximity to the particle surface, which may lead to mesh degradation. To reduce this effect, instead of pure Laplace equation, we find $\mathbf{v}_{\text{mesh}}$ as a solution of

$$\Delta(f\,\mathbf{v}_{\text{mesh}}) = 0, \tag{2.20}$$

where $f : \Omega_0(t) \to \mathbb{R}$ is an appropriately chosen scalar function that decreases with increasing distance from particle surface. A good choice for circular particles would be the inverse of (2.17). The effect of the function f is highly pronounced when a single small particle moves through a large domain as seen in Figure 2.3, where adding the function f clearly keeps the mesh quality higher after the mesh movement. In this case, low mesh quality means that the mesh contains elongated or similarly distorted triangles. This may after a few iterations of mesh movement lead to triangle overlapping, which overwhelmingly leads to incorrect solution or outright non-convergence. However, the addition of function f may not be that useful for systems with multiple particles as the relative movement among the particles is the prevalent cause of mesh degradation. In Figure 2.4 two particles pass each other and flatten the elements in between. This problem can not be easily solved by a better choice of mesh velocity, especially systems with higher number of particles or systems where particle travels significantly larger distance than the particle size.

To solve the mesh degradation in a more robust way, we introduce remeshing, i.e. the process of creating a new mesh to replace the mesh used in a previous time step. In our implementation, the new mesh is created after a fixed amount of steps. This remeshing interval can be adjusted to reflect the complexity of a given problem. In general, the interval should be small enough to mitigate the mesh degradation as seen in Figures 2.3 and 2.4. But at the same time, to use the solution from the previous time step (e.g. in the backward difference (2.15)) after a new mesh was created, we need to project the function on a different space as the mesh vertices and subsequently the basis functions of the Lagrange elements are different on the new mesh. This introduces an interpolation error every time we remesh, which motivates us to make the remeshing period as large as possible. In our implementation, we use `admesh` library created by Fara [2022]. Instead of creating a new mesh altogether, `admesh` modifies the existing mesh by adding and removing vertices and edges to fix the flattened elements. This way, many

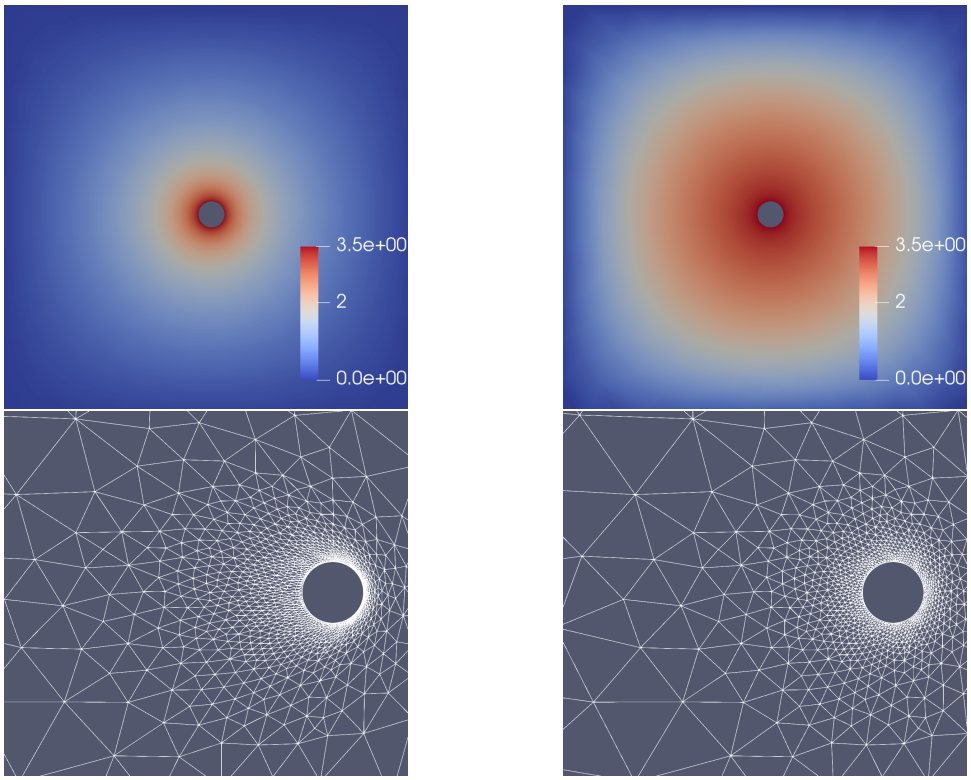

Figure 2.3: The comparison of the mesh velocity $\mathbf{v}_{\text{mesh}}$ obtained as the solution of equation (2.18) (left) and $\mathbf{v}_{\text{mesh}}$ obtained as the solution of (2.20) for f chosen as inverse of (2.17) for $a = 1$, $b = 1$ and $c = \infty$ (right). We show the magnitude of $\mathbf{v}_{\text{mesh}}$ in the first step of the computation (top) and the mesh after 25 steps of the particle moving right (bottom). Triangles around the particle on the right preserve their shape better that to the particle on the left, where the triangles are more distorted.

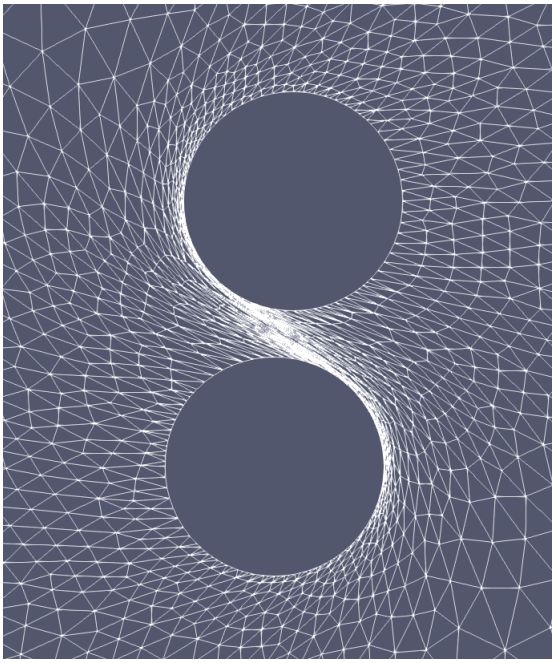

Figure 2.4: The mesh deformation resulting from two circular particles moving in opposite directions close to each other. The upper particle moves to the left, the lower moves to the right.

elements stay intact, which reduces the error caused by the projection.

We also use `admesh` to create the initial mesh. The mesh resulting from a subdivision process described in previous subsection is used as a starting point, which already approximates the particle boundaries with a sufficient degree of accuracy. This raw mesh is then modified by `admesh` to create a higher quality mesh satisfying the requirements on the element sizes. The difference between raw mesh and mesh created by `admesh` is shown in Figure 2.5.

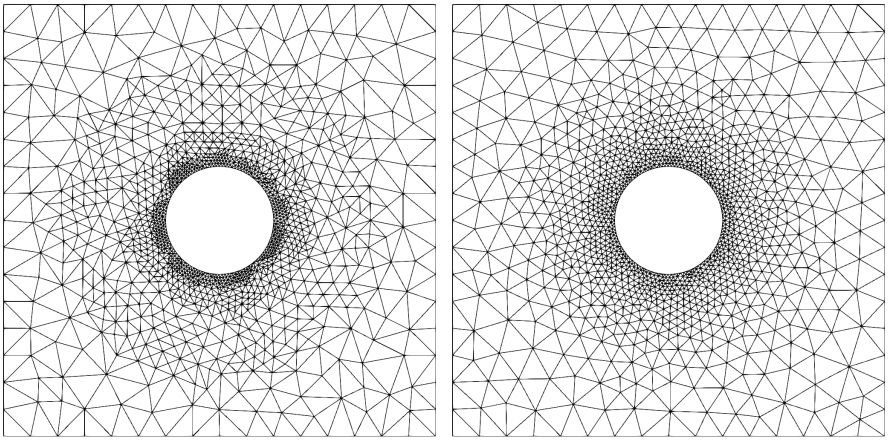

Figure 2.5: The raw mesh created by subdivisions (left) accurately describes the particle boundary. This mesh is modified by `admesh` with constraint (2.17) (fulfilled with some tolerance) to create a new mesh of higher quality (right), i.e. containing triangles with high ratio between the radii of the inscribed and the circumscribed circle. Some triangles near the outer boundary are common for both meshes as there was no necessity to update them.

2.2.3 Algorithm high-level overview

As all key parts of our method are described in the previous sections, we can now turn our focus to a high-level overview of the order in which the individual steps are performed. Before we start solving the problem, we first create the raw mesh as described in the previous subsection. In the initial step, this mesh is refined by `admesh` and all function spaces are defined on the refined mesh. With all spaces prepared, we formulate the equations and prescribe the boundary and initial conditions.

Let us now assume that we have a solution from a previous step denoted by $\mathbf{v}^{(n-1)}$, $\mathbf{V}_i^{(n-1)}$, $p^{(n-1)}$ and $\omega_i^{(n-1)}$. In the first step, the initial condition is used instead. In the current step the following operations are preformed.

Step 1. If the amount of steps since previous remesh is higher than given value, we create a new mesh and project all needed functions to the new mesh.

Step 2. We solve the fluid problem (2.13) to obtain $\mathbf{v}^{(n)}$, $p^{(n)}$, $\mathbf{V}_i^{(n)}$ and $\omega_i^{(n)}$ for $i = 1, \ldots, N$. In this step, we use the solution and the mesh movement from the previous time step.

Step 3. Solution obtained in Step 2 is used as a boundary condition to obtain the mesh velocity $\mathbf{v}_{\text{mesh}}$ from the equation (2.18) or (2.20).

Step 4. We calculate the future positions and rotations of all particles according to equations (2.8). The equations are discretized via explicit Euler scheme

$$\mathbf{X}_i^{(n+1)} := \mathbf{X}_i^{(n)} + \Delta t\, \mathbf{V}_i^{(n)}, \quad \theta_i^{(n+1)} := \theta_i^{(n)} + \Delta t\, \omega_i^{(n)}. \tag{2.21}$$

We keep track of particle position and rotation independently of mesh movement as the position and rotation values are important to e.g. mark the boundaries while remeshing or prescribe the boundary condition on the particle surface.

Step 5. We use the `ALE.move()` function to move the mesh vertices according to the mesh displacement $\Delta t\, \mathbf{v}_{\text{mesh}}$.

This sequence is then repeated until the end time T is reached.

2.2.4 The source code

The source code of our implementation is available publicly in the following URL: `https://github.com/Hruza/Fluid-Particle-ALE`

3. Benchmarks and examples

In this chapter we present multiple simple problems solved by our method to show the reliability of the method. We choose examples in which the results obtained using our method can be compared to results presented in an article, computed analytically or numerically using different, well trusted, method. In the end, we show a few more examples to present the capabilities of our method.

3.1 Heavy ball in a channel flow

In this example we replicate the flow around cylinder benchmark described in Schäfer et al. [1996]. In two dimensions, a circle is placed inside a rectangular domain and a parabolic velocity profile is prescribed at the inlet and the lift and drag acting on the circle is recorded. To be more specific, we want to solve the incompressible homogeneous Navier-Stokes equations

$$\begin{aligned} \operatorname{div} \mathbf{v} &= \mathbf{0}, \\ \rho\left(\frac{\partial \mathbf{v}}{\partial t} + (\mathbf{v}\cdot\nabla)\mathbf{v}\right) &= \operatorname{div} \mathbb{T}, \\ \mathbb{T} &= -p\mathbb{I} + 2\mu\mathbb{D}. \end{aligned} \tag{3.1}$$

in the domain $\Omega_0 = (0\,\mathrm{m}, 2.2\,\mathrm{m}) \times (0\,\mathrm{m}, 0.41\,\mathrm{m}) \setminus \mathrm{B}$, where B is a ball with a center $(0.2\,\mathrm{m}, 0.2\,\mathrm{m})$ and radius $0.05\,\mathrm{m}$. We split the boundary into four parts, the left edge Γ_{in}, the right edge Γ_{out}, the union of the top edge, bottom edge and the ball surface Γ_{D}. The following boundary conditions are prescribed

$$\mathbf{v} = 0 \qquad \text{on } \Gamma_{\mathrm{D}}, \tag{3.2}$$

$$\mathbf{v} = \mathbf{v}_{\mathrm{in}} \qquad \text{on } \Gamma_{\mathrm{in}}, \tag{3.3}$$

$$(\mathbb{T}\mathbf{n})_x = 0 \qquad \text{on } \Gamma_{\mathrm{out}}, \tag{3.4}$$

where $\mathbf{v}_{\mathrm{in}} = \left(\frac{4Uy(0.41-y)}{0.41^2}, 0\right)$. The shape of the domain and boundaries is shown in Figure 3.1. The parameters are chosen as follows

$$\rho_{\mathrm{fluid}} = 1\,\frac{\mathrm{kg}}{\mathrm{m}^3}, \quad \mu = 0.001\,\mathrm{Pa}\cdot\mathrm{s}, \quad \mathrm{U} = 0.3\frac{\mathrm{m}}{\mathrm{s}}.$$

We are interested in the values of the coefficient of drag C_{D} and the coefficient of lift C_{L}, which is defined as follows

$$C_{\mathrm{D}} = \frac{2F_x}{(2R)\rho_{\mathrm{fluid}}\overline{U}^2}, \quad C_{\mathrm{L}} = \frac{2F_y}{(2R)\rho_{\mathrm{fluid}}\overline{U}^2}, \tag{3.5}$$

where F_x and F_y is the force acting on the cylinder in the direction of x and y coordinate respectively, and $\overline{U}$ is the mean inflow velocity. In our case, the mean velocity is $\overline{U} = 0.2\,\frac{\mathrm{m}}{\mathrm{s}}$. This value is calculated from the following definition

$$\overline{U} = \frac{1}{|\Gamma_{\mathrm{in}}|}\int_{\Gamma_{\mathrm{in}}} (\mathbf{v}_{\mathrm{in}})_x \, dx.$$

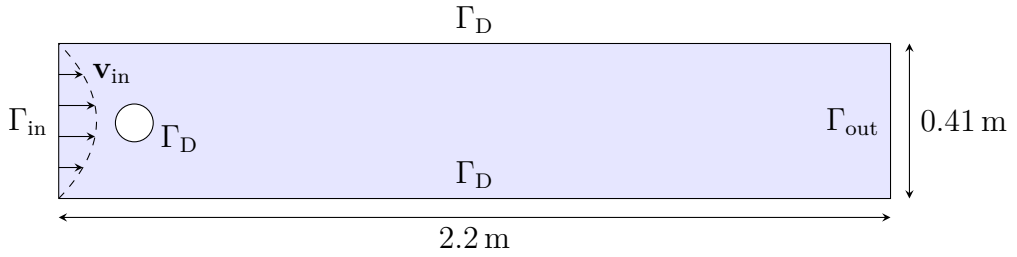

Figure 3.1: The domain Ω_0 (in blue) is a rectangle with a circle cut out. We prescribe a parabolic velocity $\mathbf{v}_{in}$ on the left edge Γ_{in}. We assume a zero traction boundary condition at the outlet Γ_{out} and no-slip boundary condition on the remaining three parts of the boundary, denoted together as Γ_D.

To validate the reliability of our method, we approximate this benchmark problem with a problem with moving boundary Γ_D. Instead of prescribing the Dirichlet boundary condition on the obstacle surface, we employ our method described in the previous chapter. We assume that the solution of such problem would be close to original benchmark problem for sufficiently large ρ_{ball}. The initial velocity of the ball is set to zero. The mesh used in the benchmark is denser around the ball as shown in Figure 3.3a. Ball with lower density will be pushed by the flow, we can therefore expect decrease of drag coefficient as the relative velocity of the fluid will be lower. The time step is set to $\Delta t = 0.02\,\mathrm{s}$ and to prevent mesh quality degradation, we create new mesh after each 10 steps for $\rho_{ball} = 10\,\frac{\mathrm{kg}}{\mathrm{m}^3}$ and each 50 steps for $\rho_{ball} = 10^2\,\frac{\mathrm{kg}}{\mathrm{m}^3}, 10^3\,\frac{\mathrm{kg}}{\mathrm{m}^3}$, for $\rho_{ball} = 10^5\,\frac{\mathrm{kg}}{\mathrm{m}^3}$ no remeshing is needed. However, by remeshing we introduce the interpolation error, which arises when the solution from previous step is projected on the new mesh. This effect should be reduced by the use of `admesh` library. The new mesh created by the `admesh` library preserves as many vertices from previous step as possible and changes only the most distorted cells.

$\rho_{ball}\ [\frac{\mathrm{kg}}{\mathrm{m}^3}]$	C_D	C_L	position [m]
10	0.425554	-0.0123286	1.46037
10^2	3.11464	0.0080869	0.512656
10^3	5.11539	0.0127381	0.237611
10^5	5.56504	0.0106767	0.200386

Table 3.1: The drag and lift coefficients at time $t = 7\,\mathrm{s}$ measured by integrating the acting force over the ball surface. In the last column there is the x position of the ball center at time $t = 7\,\mathrm{s}$. The initial position is $y = 0.2\,\mathrm{m}$, we can clearly see the movement decrease withe particle size, which in turn increases the drag coefficient.

The resulting numerical solutions converge to a steady state as indicated by the drag and lift coefficient in Figure 3.2. As we are interested in the steady flow, we investigate the resulting coefficients at time $t = 7\,\mathrm{s}$. The Schäfer et al. [1996] observed the coefficient of drag between 5.57 and 5.59 and the coefficient of lift between 0.0104 and 0.0110. Values from our method are close to this range for large enough ball density, the precise values are shown in Table 3.1. The main reason for slight deviation from expected range seems to be slight movement of

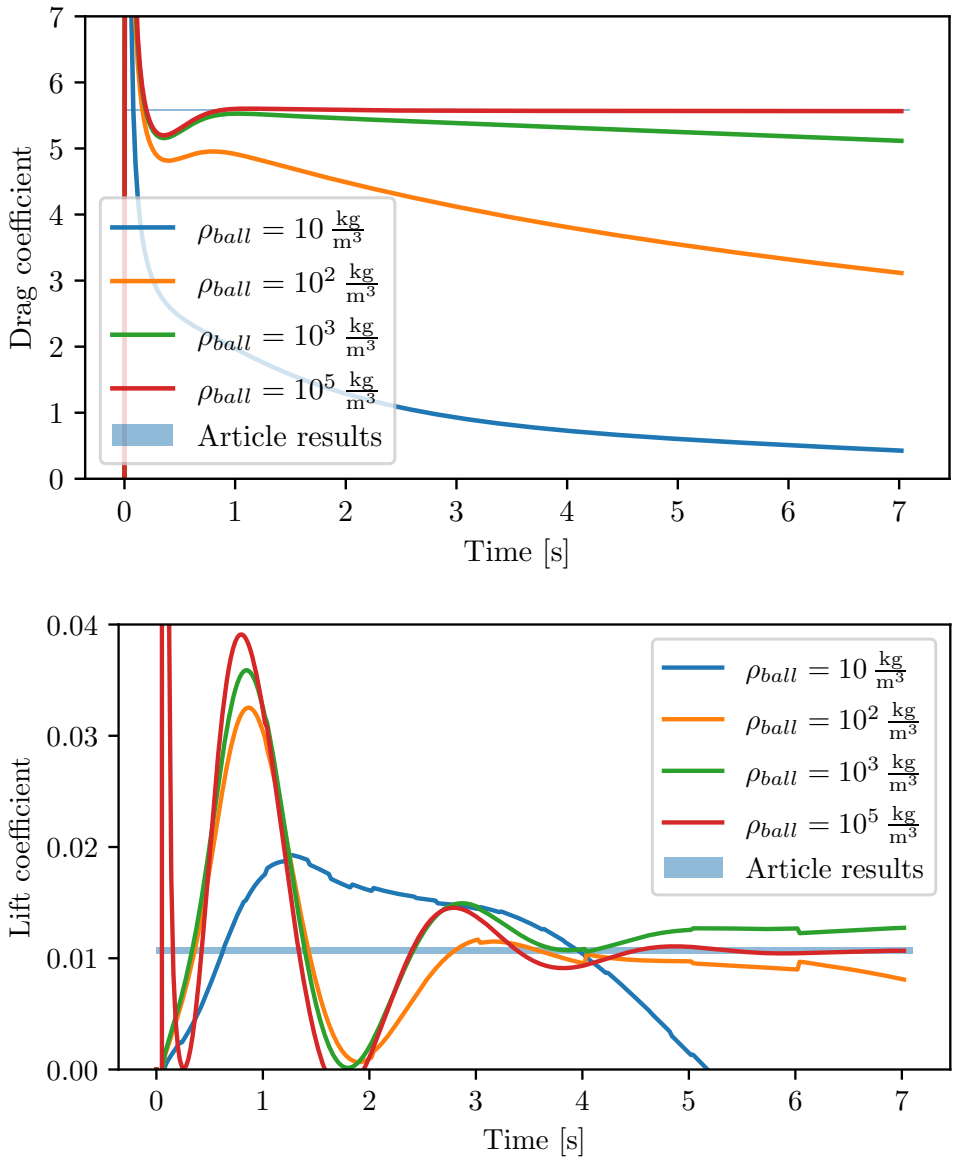

Figure 3.2: The convergence of the coefficient of drag (top) and lift (bottom). A clear convergence to the theoretical values with rising ball density can be observed. As the lift coefficient is relatively small, we can see slight jumps in calculated value due to interpolation error in remeshing.

even the heavies particles. This effect should make the force slightly lower as the relative velocity of the fluid is also lower. For the heaviest particle we have $C_{\text{D}} = 5.5712$ at time $t = 3\,\text{s}$, in this time the flow is already rather stationary, and the ball does not move as much as at $t = 7\,\text{s}$. From the results of this benchmark, we can conclude, that our method behaves as expected in this benchmark.

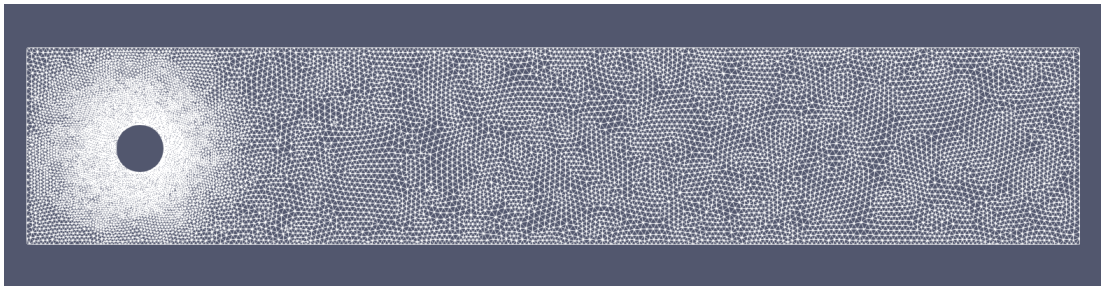

(a) Mesh used in the benchmarks. The mesh is more dense around the ball, where the velocity field is expected to be the most complicated.

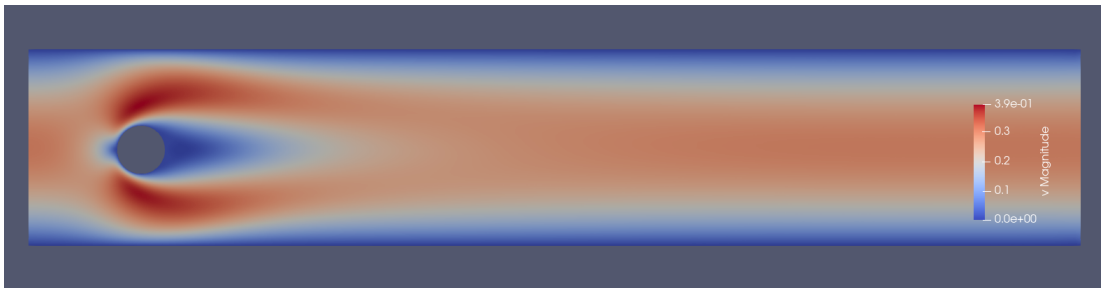

(b) The velocity field at time $t = 7\,\mathrm{s}$.

Figure 3.3: The solution of the channel benchmark computed by the method for the ball with density $\rho_{\mathrm{ball}} = 1000\,\frac{\mathrm{kg}}{\mathrm{m}^3}$.

3.2 Lubrication force

Similarly to the previous section we investigate the forces acting on a particle in a fluid flow. However, instead of the drag force, we observe the force acting on a particle near a domain boundary. More specifically, there is a force slowing down a particle approaching a flat boundary with a no-slip boundary condition in a fluid described by the Navier-Stokes equation. The asymptotic behavior of this force was described in Leal [1992] and has the following formula

$$F_{\mathrm{L}} = 3\sqrt{2}\pi\mu \left(\frac{R}{h}\right)^{\frac{3}{2}} \frac{dh}{dt}, \quad \text{as } h \to 0, \tag{3.6}$$

where R is the radius of the ball particle and h the distance between the wall and the flat surface (the distance of two closest points). We refer to the force caused by the proximity to a boundary as the lubrication force. Due to this force, a rigid ball moving towards the surface in direction perpendicular to the flat surface will stop before any contact occurs. Furthermore, a rigid ball does not bounce off in such circumstances, i.e. the ball never moves away from the surface. This phenomenon is described in detail by Gravina et al. [2022].

The problem solved with our method can be described as follows. We want to solve the Navier-Stokes equation inside the domain $\Omega_0 = (0, W) \times (0, H) \setminus B$, where B is initially a circular particle with center in $(\frac{W}{2}, h_0)$ and with radius R. The no-slip boundary condition is prescribed on the outer boundary of Ω_0

$$\mathbf{v} = \mathbf{0} \quad \text{on } \partial\Omega_0 \setminus \partial B. \tag{3.7}$$

The model is then formulated as presented in the previous section. In particular, the no-slip boundary condition is prescribed on the ball surface (the velocity is

zero with respect to the rigid movement of the ball). The initial ball velocity is set to $\mathbf{V}(0) = (V_0, 0)$. To have a comparison, we also compute the same problem with zero traction boundary condition on $\Omega_0 \setminus \partial B$ instead of no-slip

$$\mathbb{T}n = \mathbf{0}, \quad \text{on } \partial\Omega_0 \setminus \partial B.$$

In this case, the circular particle is initially placed further from the boundary for the purpose of eliminating the lubrication forces caused by the proximity to a boundary. As the lubrication force is negligible in the zero traction case, we can assume that all drag forces are caused by the viscosity of the fluid. Therefore, if we subtract the force in the zero traction case from the forces in the no-slip case, we expect to obtain a force described as (3.6). However, we can not directly subtract these values as the particles in both problem move in a different rate and therefore the drag force due to viscosity is also different.

Let us denote the y component of force acting on the particle in the no-slip problem by F^{no} and in the zero traction problem by F^{free}. We assume that the force F^{no} is a sum of the drag force F_{D}^{no} and the lubrication force F_L^{no}, where F_{D}^{no} is proportional to the squared velocity, i.e.

$$F^{\text{no}} = F_{\text{D}}^{\text{no}} + F_L^{\text{no}}, \quad F_{\text{D}}^{\text{no}} \sim v_y^2.$$

In particular, as shown previously in equations (3.5), $\frac{F_{\text{D}}^{\text{no}}}{v_y^2}$ should be a constant that depends mostly on the variables common in both systems. And thus, as F^{free} is assumed to have the same properties, we obtain

$$\frac{F_{\text{D}}^{\text{no}}}{(v_y^{\text{no}})^2} - \frac{F^{\text{free}}}{(v_y^{\text{free}})^2} \approx 0.$$

Finally, this gives us a following identity.

$$\left(\frac{F^{\text{no}}}{(v_y^{\text{no}})^2} - \frac{F^{\text{free}}}{(v_y^{\text{free}})^2}\right) v_y^{\text{no}} \approx \frac{F_L^{\text{no}}}{v_y^{\text{no}}} = 3\sqrt{2}\pi\mu \left(\frac{R}{h}\right)^{\frac{3}{2}}. \tag{3.8}$$

We chose the following parameters for the presented simulation

$$w = h = 20\text{m}, \quad \text{R} = 0.5\,\text{m}, \quad \text{h}_0 = 5\,\text{m}, \quad \Delta\text{t} = 0.02\,\text{s}, \quad \text{V}_0 = 5\frac{\text{m}}{\text{s}},$$

as shown in Figure 3.4. The qualitative behavior matches the expectations, the ball completely stops in the no-slip problem as shown in Figure 3.5. The difference between F^{no} and F^{free} also matches the theory predicted by 3.6 quite well as shown in Figure 3.6. Let us take a close look at the quality of the approximation. Let us use the least squares method to approximate the left-hand side of (3.8) with a curve in a form ah^{-b} for some constants $a \in \mathbb{R}$ and $b \in \mathbb{R}$. The results are presented in Table 3.2. We can clearly see that the approximation gets closer to theoretical values with increasing domain size and decreasing time step. The error of our best approximation may be caused by the discretization error or difference between the two compared problems, as it is not possible to compare the results directly.

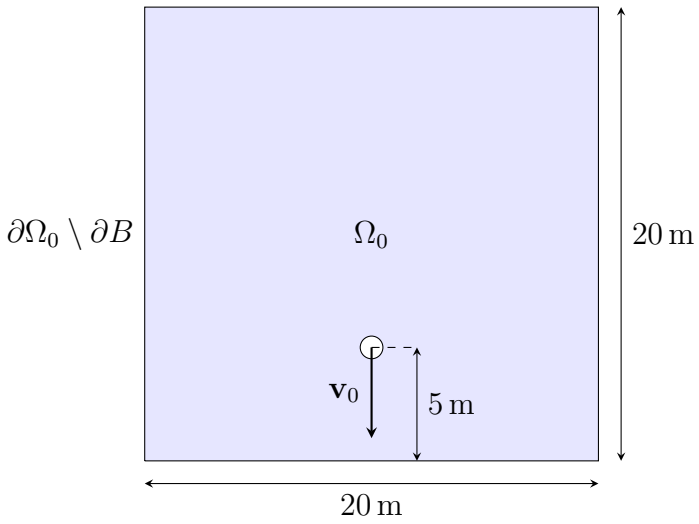

Figure 3.4: We start with a square domain with particle in the distance of 5 m from the bottom edge. The particle has initial velocity of 5 $\frac{\text{m}}{\text{s}}$ in the direction of negative y coordinate, i.e. towards the bottom edge.

Theory	Calculated 10x10 square $\Delta t = 0.02\,\text{s}$	Calculated 20x20 square $\Delta t = 0.02\,\text{s}$	Calculated 20x20 square $\Delta t = 0.01\,\text{s}$
$0.4712h^{-1.5}$	$0.629h^{-1.23}$	$0.570h^{-1.29}$	$0.568h^{-1.34}$

Table 3.2: A comparison of curves obtained using the least square method for various simulation variables.

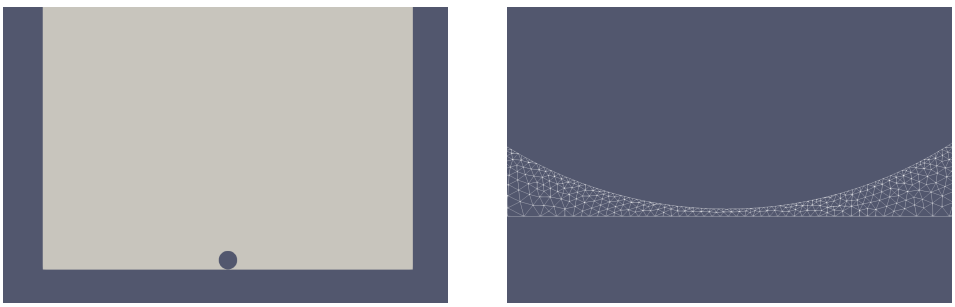

Figure 3.5: The solution with a no-slip boundary condition at time $t = 5\,\text{s}$. The circular particle completely stops around $t = 2.25\,\text{s}$ and we see no significant particle movement after this time. The particle is divided from the boundary by two layers of elements.

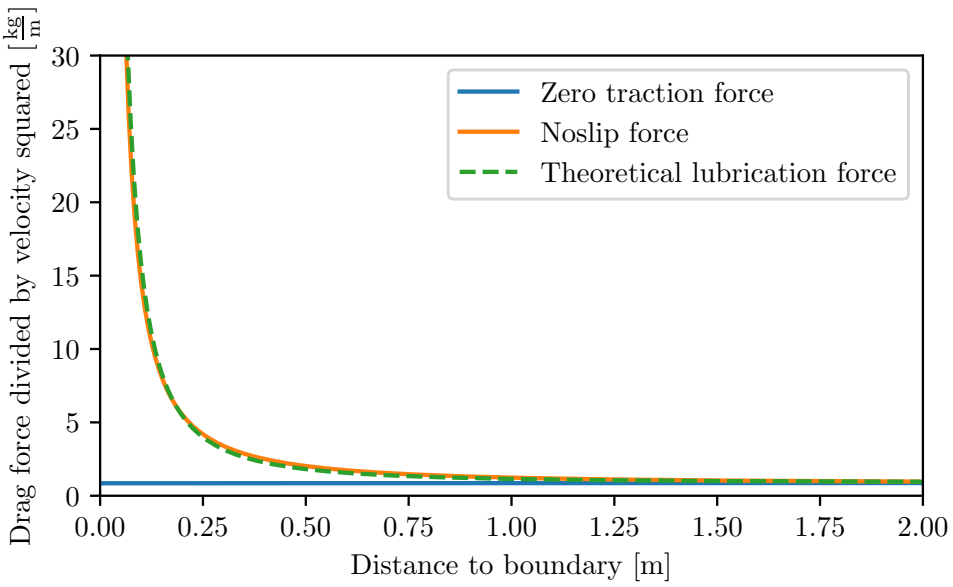

Figure 3.6: The dependence of the y component of drag force divided by the y component of ball velocity on the distances from the boundary. We compare two values, $\frac{F^{\text{no}}}{\left(v_y^{\text{no}}\right)^2}$ (blue) and $\frac{F^{\text{free}}}{\left(v_y^{\text{free}}\right)^2}$ (orange). The dashed line represents the force predicted by (3.6), to be more specific, we use the following value derived from equation (3.8): $\frac{F^{\text{free}}}{\left(v_y^{\text{free}}\right)^2} + 3\sqrt{2}\pi\mu\left(\frac{R}{h}\right)^{\frac{3}{2}}\frac{1}{v_y^{\text{no}}}$. We observe that the theory matches our calculations quite well.

3.3 Conservation of momentum

For systems with more particle interactions as a rather basic benchmark, we investigate the conservation of total linear momentum. Let us first define the total linear momentum in domain Ω

$$P(t) = \int_{\Omega_0(t)} \rho \mathbf{v} \, d\mathbf{x} + \sum_{i=1}^{N} m_i \mathbf{V}_i. \tag{3.9}$$

We expect the total momentum of the system P, for a zero traction boundary condition prescribed on the outer boundary, to be independent of time as there are no outside forces acting on the fluid. However, this is only true in Lagrangian sense if we consider total momentum of the material in reference configuration. In our case, we have to include the momentum that is exchanged with environment via mass exchange through the outer boundary Γ

$$\frac{dP}{dt} = -\int_{\Gamma} \rho \left(\mathbf{v} \cdot \mathbf{n}\right) \mathbf{v} \, dS, \tag{3.10}$$

$$P(t) = -\int_0^t \int_{\Gamma} \rho \left(\mathbf{v}(\tau) \cdot \mathbf{n}\right) \mathbf{v}(\tau) \, dS \, d\tau + P(0). \tag{3.11}$$

Of course, we can not expect that the linear momentum conserves exactly in the numerical computation (due to the approximation error and the rounding error). In particular, we can expect the error to gradually increase as the error may incrementally add up. Therefore, we will observe the initial momentum $P(0)$ from (3.11) and check if the momentum conservation improves with decreasing time step size.

We define an example problem, let $\Omega = (0\,\mathrm{m}, 10\,\mathrm{m}) \times (0\,\mathrm{m}, 10\,\mathrm{m})$ be a square domain and let us add two circular particles with radius $r = 0.4\,\mathrm{m}$ into the system, the domain Ω with the two particles cut out is denoted by Ω_0. The first circle denoted by P_1 is located in the left half of the domain and the second particle denoted by P_2 is then placed to the right of the first particle slightly lower than P_1. The initial distribution is described in detail in Figure 3.7. The initial velocity of the fluid and particle P_2 is set to $\mathbf{0}$, but the velocity of the particle P_1 is set to $\mathbf{V}_0 = (5, 0)\,\frac{\mathrm{m}}{\mathrm{s}}$. Although it seems that the particle P_1 may hit particle P_2, the contact should never happen for small enough time step due to the lubrication force described in the previous section. On the outer boundary denoted by Γ_0 we prescribe the zero traction boundary condition

$$\mathbb{T}\mathbf{n} = \mathbf{0} \quad \text{on } \Gamma_0.$$

The parameters of the system are chosen as follows

$$\rho_{\text{fluid}} = 1\,\frac{\mathrm{kg}}{\mathrm{m}^3}, \quad \rho_{\text{particle}} = 4\,\frac{\mathrm{kg}}{\mathrm{m}^3}, \quad \mu = 0.1\ \mathrm{Pa} \cdot \mathrm{s}.$$

We ran the simulation for three different time step sizes Δt: $0.04\,\mathrm{s}$, $0.02\,\mathrm{s}$ and $0.01\,\mathrm{s}$. In all cases the initial mesh was identical and the number of degrees of freedom was around 10^5. The simulation result for $\Delta t = 0.02\,\mathrm{s}$ are shown in Figure 3.8. We can see that the momentum of particle P_1 is converted into the momentum of the surrounding fluid, which in turn moves particle P_2 as

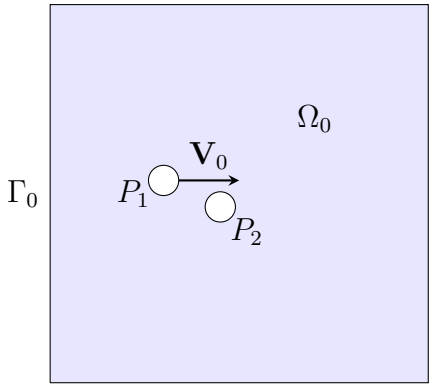

Figure 3.7: The initial state of the problem. The coordinates of particle centers are $\mathbf{X}_1 = (3\,\mathrm{m}, 3.35\,\mathrm{m})$ and $\mathbf{X}_2 = (4.5\,\mathrm{m}, 4.65\,\mathrm{m})$. The initial particle position is chosen in such a way, that the particles would barely overlap if we would move P_1 horizontally above P_2.

both particles get close to each other.The mesh and velocity magnitude in some steps are shown in Figure 3.8. Regarding the quantitative result, the total linear momentum in the direction of the x-axis can be seen in Figure 3.9. We can see that in all cases the total momentum conserves quite well. Moreover, the maximum deviation of total momentum from the correct value is lower for lower time step. We also checked, that the error does not meaningfully decrease with the increase of mesh density.

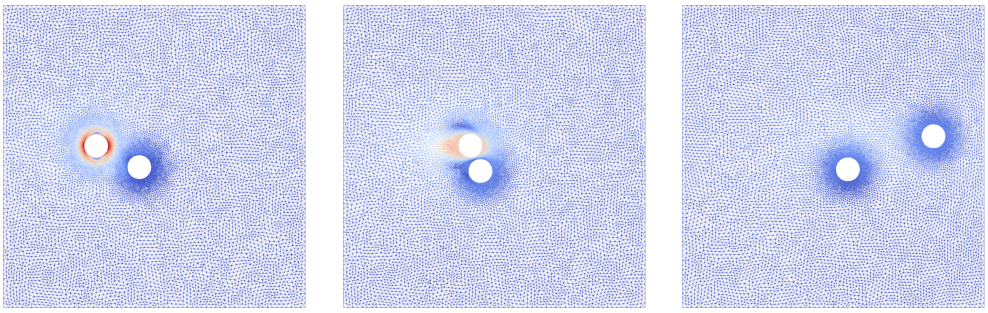

Figure 3.8: The result of numerical simulation at time $t = 0.02\,\mathrm{s}$ (left), $t = 0.44\,\mathrm{s}$ (middle) and $t = 5\,\mathrm{s}$ (right). The increase of mesh density around the particle surface is clearly visible. The color of mesh edges represents the velocity magnitude on a scale from $0\,\frac{\mathrm{m}}{\mathrm{s}}$ (blue) to $5\,\frac{\mathrm{m}}{\mathrm{s}}$ (red).

Analogously, we can measure the total angular momentum of the system, but in this case, the angular momentum depends on a point against which we measure. If we denote this point by $\mathbf{x}_\mathrm{c}$, the total angular momentum in this point should be conserved

$$L(t) = \int_{\Omega_0(t)} \rho(\mathbf{x} - \mathbf{x}_\mathrm{c}) \times \mathbf{v}\, d\mathbf{x} + \sum_{i=1}^{N} \frac{1}{2} m_i r_i^2 \omega_i + \sum_{i=1}^{N} m_i (\mathbf{X}_i - \mathbf{x}_\mathrm{c}) \times \mathbf{V}_i, \qquad (3.12)$$

where r_i is the radius of i-th particle. The angular momentum can be divided into three parts corresponding to the three terms in (3.12), the contribution of

the fluid movement, particle rotation and particle translation. Analogously to the previous example, we have to account for the angular momentum flowing through the outer boundary, this gives us

$$L(t) = -\int_0^t \int_\Gamma \rho \left(\mathbf{v}(\tau) \cdot \mathbf{n}\right) \left(\mathbf{x} - \mathbf{x}_c\right) \times \mathbf{v}(\tau)\, dS\, d\tau + L(0). \tag{3.13}$$

We measured the total angular momentum in the center and in the origin (bottom left corner of Ω), in both cases the angular momentum is well-preserved and the error decreases with the decrease of time step size. This effect can be clearly seen in Figure 3.10 showing the total angular momentum in the center.

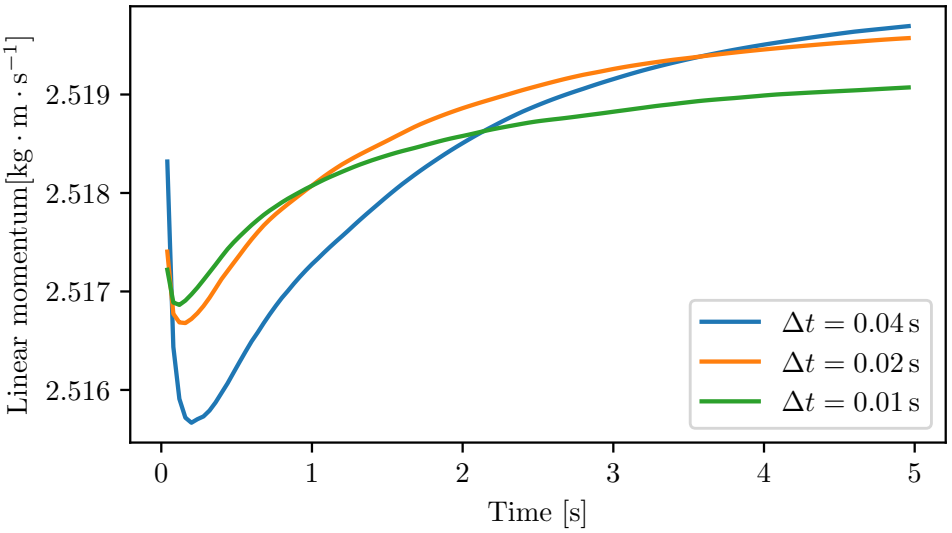

Figure 3.9: The total linear momentum in the direction of the x axis for three different time step choices. All cases vary very slightly, the difference betwee largest and smallest value of the momentum is under $0.005\,\mathrm{kg} \cdot \mathrm{m} \cdot \mathrm{s}^{-1}$, but lower time step clearly results in lower variance. The behavior of y-component of linear momentum is similar.

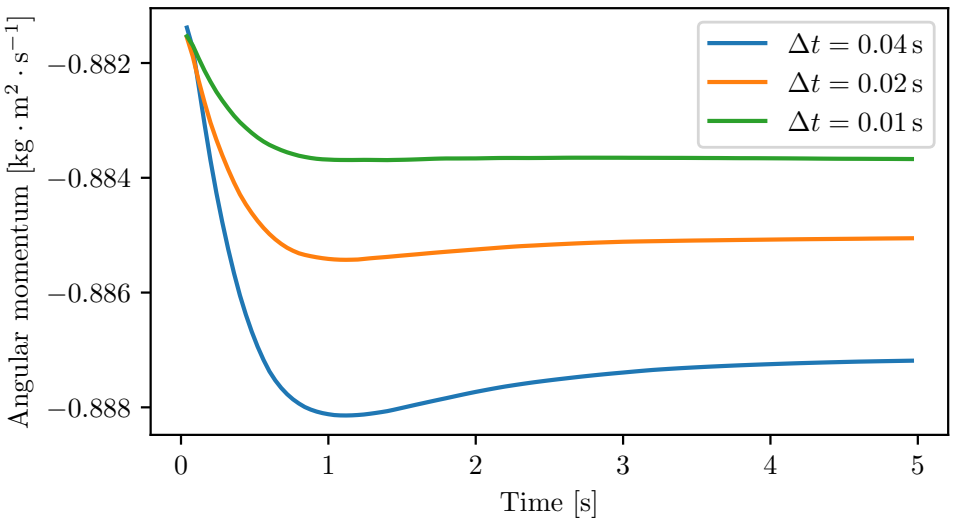

Figure 3.10: The total angular momentum for three different time steps, the angular momentum is measured in the center of domain Ω, $\mathbf{x} = (5\,\mathrm{m}, 5\,\mathrm{m})$. The scale of the y-axis shows that even for the worst case the angular momentum changes only very slightly and the improvement as the time step decreases is clear.

3.4 Other examples

In this section, we discuss the versatility of our model. In particular, we describe the technical limitations to the shape and count of particles that our model is able to simulate.

3.4.1 Particle shape

In all the previous benchmarks we assumed circular particles. However, the model described in Chapter 2 works for almost any particle shape[1]. The particles are not modified or regenerated during computation. Therefore, any particle can be simulated as long as we can create the initial mesh with a desired particle shape. Although this is true in theory, in practice we have to define the particle boundary after each remeshing to prescribe the boundary condition. This is easily done if there exist a continuous function ψ such that ψ is negative inside the particle and positive outside. For circular particles this function is the distance from the center

$$\psi_i(\mathbf{x}) = \|\mathbf{x} - \mathbf{X}_i\| - r_i.$$

This function can be simply generalized to allow for elliptical particles using an appropriately chosen matrix A

$$\psi_i(\mathbf{x}) = \|A(\mathbf{x} - \mathbf{X}_i)\| - r_i.$$

We tested the simultaion of elliptical particles on the following problem, let Ω_0 be a rectangular domain with two ellipses next to each other cut out. We then

[1] In theory, the particles do not even need to be connected and we can consider e.g. rigid "diparticles" or "quadruparticles" that consist of multiple disjoint components.

prescribed the initial angular velocities $\omega_1 = 15\,\mathrm{s}^{-1}$ and $\omega_2 = -15\,\mathrm{s}^{-1}$. The solution at four different times is presented in Figure 3.11. We can see that the angular velocity of the ellipses decreases (velocity near boundary is lower) and in turn the fluid velocity increases in most parts of the domain.

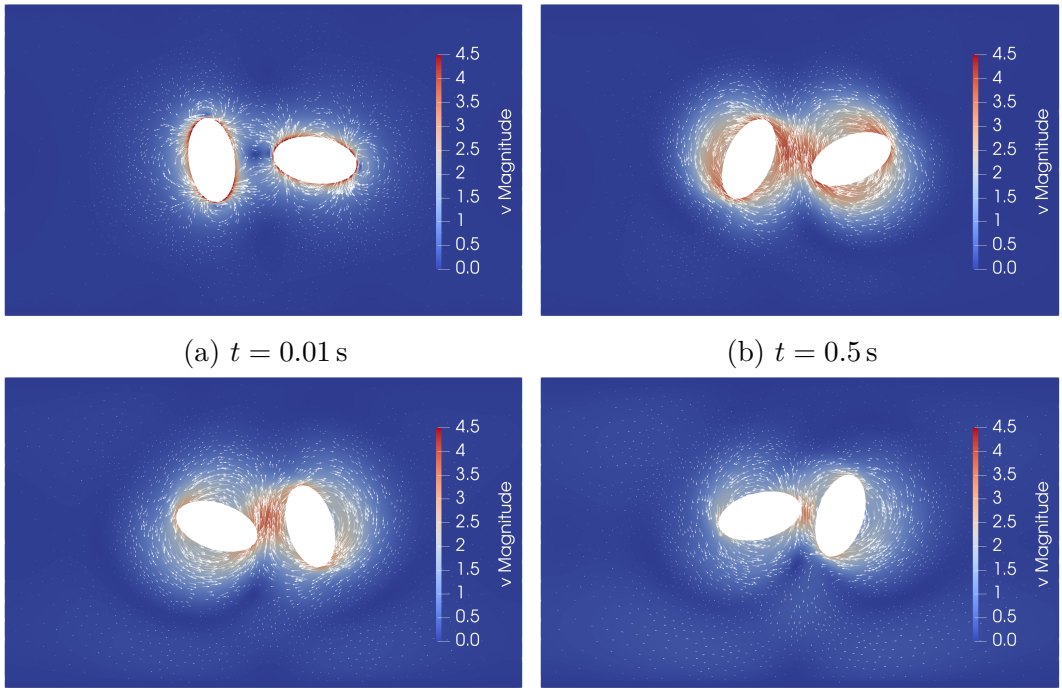

(a) $t = 0.01\,\mathrm{s}$ (b) $t = 0.5\,\mathrm{s}$

(c) $t = 1\,\mathrm{s}$ (d) $t = 1.5\,\mathrm{s}$

Figure 3.11: The result of numerical simulation of rotating elliptical particles at four different times.

3.4.2 Particle count

In all previous examples, no more than two particles are present, but similarly to the particle shape, the model described in Chapter 2 allows for arbitrary number of particles. In theory, the maximal number of particles is limited only by the domain size. However, there are some limiting factors in the numerical computation. First of all, to describe the particle boundary and the flow around it accurately, we use denser mesh near the boundary surface. Although adding particles decreases the size of the computational domain, the number of triangles in the mesh usually increases with each particle, because the number of elements around particle surface vastly outnumber the number of elements that would be in the place of the particle. Examples with up to 40 particles are shown in the following chapter.

4. Results

In this chapter, we investigate the effect of shear thinning caused by the addition of rigid particles to a Newtonian fluid, which on itself does not possess a shear thinning property. We start with a problem of the Couette flow between two infinite parallel planes induced by a no-slip boundary condition on one plane and prescribed velocity in the tangent direction on the other. We are then able to define and calculate the apparent viscosity and investigate the change of viscosity according to change of velocity and particle distribution. However, we show that this approach is not suitable for the numerical calculation of apparent viscosity, because simulating the system over long periods of time is not possible. We therefore improve our model to mitigate this problem. In particular, we formulate a similar Couette flow problem between two cylinders, that allows us to measure apparent viscosity over long time intervals.

Before we start with the model implementation, we define the shear thinning property.

Definition 1. *The fluid is said to have a shear thinning property if the generalized viscosity decreases under a shear rate. For two-dimensional problem, we define the generalized viscosity* μ_g *as*

$$\mu_g = \frac{T_{12}}{D_{12}},$$

where T_{12} *is the shear stress and* D_{12} *is the shear rate.*

4.1 Flow in a rectangular domain

One way to observe and quantify shear thinning is to measure the apparent viscosity as it may be done in the experiment. Let us have two infinite horizontal planes on top of each other with a space in between of height h containing the observed fluid. Let us start moving the upper plane. In the Newtonian case, a force caused by the viscosity of the fluid acts against the motion of the plane. Calculating the magnitude of the boundary forces lets us define the apparent viscosity for a fluid-particle mixture. For this reason, we are interested in a Couette flow of the particle-fluid system which we proceed to formulate.

Let $\Omega = (0, l) \times (0, h)$ be a rectangular domain and let us cut out N circular particles with radius r to obtain Ω_0, a domain filled with a Newtonian fluid. The particles are clustered on the left side of Ω at $t = 0$ to leave a room for a movement on the right side. The distribution of particles in the initial cluster is one of the parameters to investigate. The following boundary conditions for the fluid velocity $\mathbf{v}$ are prescribed on the outer edges of Ω_0

$$\begin{aligned} \mathbf{v} &= \mathbf{0} \qquad \text{on } \Gamma_{\text{bottom}}, \\ \mathbf{v} &= (V, 0) \quad \text{on } \Gamma_{\text{top}}, \\ v_2 &= 0 \qquad \text{on } \Gamma_{\text{left}} \cup \Gamma_{\text{right}}, \end{aligned} \tag{4.1}$$

where Γ_{left}, Γ_{right}, Γ_{bottom} and Γ_{top} denote the corresponding outer edges as shown in Figure 4.1.

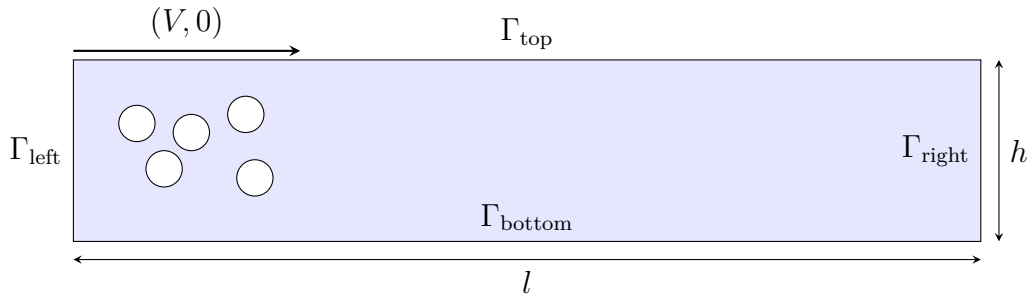

Figure 4.1: Domain used in the Couette flow problem between two planes, the particles start in a certain distribution on the left-hand side of the domain.

As this example is inspired by the flow of blood, we chose the parameters to loosely match the parameters of blood flow. Parameters in Leuprecht and Perktol [2001] are used as a baseline, but some values are modified for us to better investigate the role of particles. For example, our computational domain is much smaller than a typical blood vessel with such blood velocities. The blood cell size is taken from Lanotte et al. [2016] and the density of particles is chosen to be equal to the fluid density. The parameters used in the computation are as follows

$$\begin{aligned} \rho &= 1050\,\frac{\text{kg}}{\text{m}^3}, & r &= 4\,\mu\text{m}, \\ \mu &= 3.896 \cdot 10^{-3}\ \text{Pa}\cdot\text{s}, & h &= 100\,\mu\text{m}, \\ V &= 0.65\,\frac{\text{m}}{\text{s}}, & l &= 500\,\mu\text{m}. \end{aligned}$$

4.1.1 Apparent viscosity calculation

The apparent viscosity is calculated as presented in Lefebvre and Maury [2005]. Following the approach suggested above, let us now consider a Newtonian fluid satisfying the incompressible homogeneous Navier-Stokes equations in Ω with boundary conditions (4.1). The solution is in a form of linear velocity profile

$$\mathbf{v}(x, y) = V\frac{y}{h}\begin{pmatrix}1\\0\end{pmatrix}, \quad p(x, y) = 0. \tag{4.2}$$

We can simply verify this fact by substituting the functions to the governing equations. The continuity equation (1.2) is clearly satisfied as $\operatorname{div}\mathbf{v} = 0$. The balance of linear momentum is also satisfied, upon substituting (4.2) into the ballance of linear momentum (1.1), one indeed obtains

$$\rho\left(\frac{\partial\mathbf{v}}{\partial t} + (\mathbf{v}\cdot\nabla)\mathbf{v}\right) = -\nabla p + \mu\operatorname{div}\left(\nabla\mathbf{v} + (\nabla\mathbf{v})^T\right),$$

$$\rho\,(\mathbf{0} + \mathbf{0}) = -\mathbf{0} + \mu\operatorname{div}\begin{pmatrix}0 & \frac{V}{h}\\ \frac{V}{h} & 0\end{pmatrix} = \mathbf{0}.$$

The boundary conditions are also clearly satisfied.

We now integrate the x component of the traction over Γ_{top} and Γ_{bottom} to obtain forces F_T and F_B respectively

$$F_T = \int_{\Gamma_{top}} \mathbf{t}_x\,ds = \int_{\Gamma_{top}} \mathbb{T}\mathbf{n}\cdot\begin{pmatrix}1\\0\end{pmatrix}\,ds = \int_{\Gamma_{top}} T_{12}\,ds = \mu l\frac{V}{h}.$$

The calculation for F_T is identical except the sign of normal vector. Therefore, by subtracting the two forces, we obtain the identity

$$F_T - F_B = 2\mu l \frac{V}{h}.$$

The forces on the left-hand side can be easily obtained using direct integration over the according boundary. This leads us to the following definition of the apparent viscosity μ_{app}

$$\mu_{\text{app}} = \frac{h}{2lV}(F_T - F_B). \tag{4.3}$$

This value for fluid-particle mixture is equal to the viscosity of a hypothetical Newtonian fluid exerting the same force against the plane movement as given mixture. We assume that this value approximates μ_g from Definition 1, the decrease of apparent viscosity with shear strain is therefore interpreted as a shear thinning.

4.1.2 Numerical results

To numerically simulate the fluid-particle system, we use the method described in Chapter 2. However, we want to slightly modify the boundary conditions for the mesh velocity (2.18). Instead of $\mathbf{v}_{\text{mesh}} = 0$, we prescribe $(v_{\text{mesh}})_2 = 0$ on both Γ_{bottom} and Γ_{top}. Without this modification, we would have to deal with the mesh deformation effect presented in Figure 2.4, as the mesh remains fixed on Γ_{top} and moves with particles that have the highest velocity near Γ_{top}.

Figure 4.2: The fluid domain Ω_0 with a particle cluster in a grid (top) and distributed randomly (bottom). To obtain a random distribution, we sample points uniformly in a chosen rectangle, if a choice of a point would cause an overlap, we sample again until there is no overlap. To keep the cluster consistent between different runs, a common initial seed is chosen to initialize the random number generator.

Problem with zero initial condition

We compare two different particle distributions, a 4×5 uniform grid and a sample from random uniform distribution on rectangle. The exact initial shape of Ω_0 with the particle clusters is shown in Figure 4.2. As the initial condition, we prescribe no movement

$$\mathbf{v}(0, x, y) = \begin{pmatrix} 0 \\ 0 \end{pmatrix}, \quad \mathbf{V}_i(0) = 0, i = 1, \ldots, N.$$

Boundary velocity V is initially zero and increases linearly, until it reaches desired velocity V_0 at time $t = 0.02\,\text{ms}$. The velocity V can thus be expressed using the following formula

$$V(t) = V_0 \min\left(\frac{t}{2 \cdot 10^{-5}}, 1\right).$$

To observe shear thinning, we perform the simulation with three different boundary velocities $V_0 = 0.1$, $V_0 = 0.3$ and $V_0 = 0.65$.

The apparent viscosity measured with our method is shown in Figure 4.3. As the volume of particles is proportionally small compared to the domain size, the differences between the apparent viscosities are rather small in absolute value, but we can still see some differences between individual simulations. In particular, the particles distributed in a grid result in a smaller value of apparent viscosity, which is in line with the observations by Lefebvre and Maury [2005]. A slight apparent viscosity decrease resulting from a velocity increase corresponding to a shear thinning is indeed present. However, this effect is almost certainly caused by particle separation shown in Figure 4.5, which occurs sooner in higher velocities. We can verify this claim by comparing the apparent viscosities at similar stages of system development.

For this purpose, we investigate the dependence of the apparent viscosity on the traveled distance $d = Vt$ instead of the time directly. As d is proportional to the boundary velocity V, it is an upper estimate of the distance traveled by the fastest particle. The dependence of the apparent viscosity on d is shown in Figure 4.4. Apart from the initial time-dependent steep decrease of the apparent viscosity caused by the acceleration of the mixture, the apparent viscosity seems to depend more on d rather than V. This effect is the most apparent in the interval $(0.4\,\text{mm}, 0.6\,\text{mm})$, where the results for $V = 0.65$ align with the results for $V = 0.1$ and steadily decrease as the particles become more distant from each other.

This problem is clearly inappropriate for the apparent viscosity comparison between different boundary velocities, as either the initial acceleration or the later particle separation evolves in a different rate for each velocity.

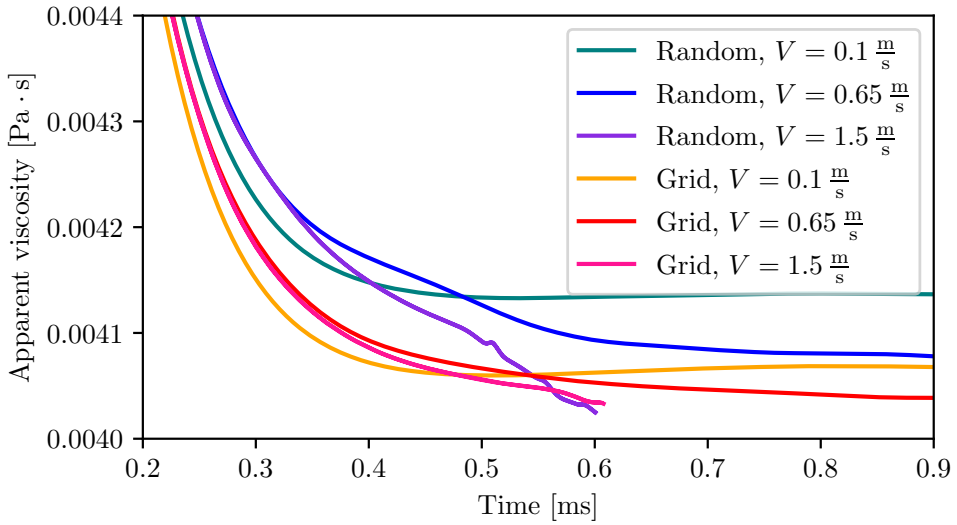

Figure 4.3: The dependence of the apparent viscosity as defined by (4.3) on time. The viscosity reduces with time as the particles start moving with the fluid. In all cases the simulation ends slightly after the first particle collides with Γ_{right}, when the mesh gets significantly distorted and the numerical method does not converge. We can clearly see the difference between particles in a grid and a random distribution as the system with particles in grid has observably lower apparent viscosity. In some parts, the apparent viscosity of faster moving system is lower or at least decreases faster, which would indicate shear thinning. However, this effect is probably caused by separation of particles, which happens faster with higher particle velocity.

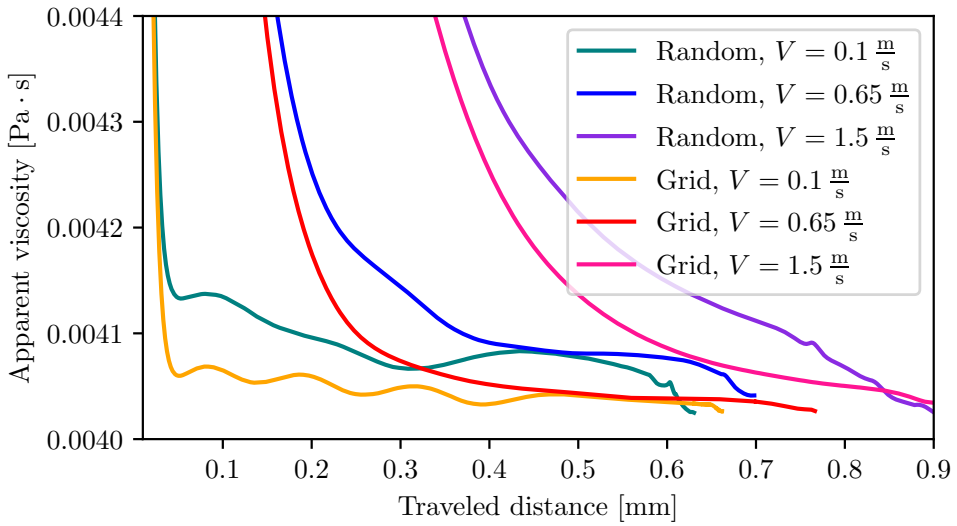

Figure 4.4: The dependence of apparent viscosity on the traveled distance defined as a product of time t and the velocity V. The initial steep decrease is caused by the acceleration of the initially stationary fluid. This process is time-dependent, thus unlike in Figure 4.3, it is not synchronized across velocities. The apparent viscosities between different velocities should be compared only after the initial steep decrease.

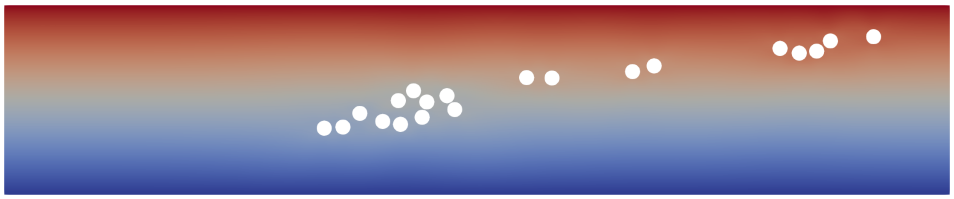

Figure 4.5: The particle cluster towards the end of simulation with $V_0 = 0.65\,\mathrm{m} \cdot \mathrm{s}^{-1}$ at $t = 0.9\,\mathrm{ms}$. The particles that are initially in a cluster get separated as each layer moves with a different speed, which decreases the apparent viscosity as the particles can move freely outside the cluster. The color indicates the velocity magnitude, which is zero at the lower boundary and equal to V_0 at the top.

Problem with initial linear velocity profile

The initial acceleration from a stationary state poses some difficulty in apparent viscosity comparison between different velocities, especially in the early stages of system development. However, we are fairly interested in the apparent viscosity in the early stages as the particles are still in a cluster and interactions between particles play a major role. We therefore present a slight modification of the Couette flow problem with linear velocity profile prescribed as the initial condition

$$\mathbf{v}(0, x, y) = V\frac{y}{h}\begin{pmatrix}1\\0\end{pmatrix}, \quad \mathbf{V}_i(0) = V\frac{(\mathbf{X}_i)_2}{h}\begin{pmatrix}1\\0\end{pmatrix}.$$

The boundary velocity V is now constant in time, which should eliminate the comparison problem described above. We also make the domain slightly narrower and the initial cluster wider to increase the relative volume of particles, and in turn increase the role of particles in the mixture response. The domain size is chosen as follows

$$h = 60\,\mu\mathrm{m}, \quad \mathrm{l} = 500\,\mu\mathrm{m}.$$

All other fluid and particle parameters are the same as in previous example.

We investigate the particles initially distributed randomly and in a grid. On top of the initial cluster with 20 particles, we simulated a problem with a wider initial cluster containing 40 particles. The example of the initial distribution in the 20 particle cluster is shows in Figure 4.6. In the apparent viscosity plot in Figure 4.7, we can see an observable difference between the two types of initial clusters, and more notably, there is also significant increase in viscosity with increased number of particles. However, we do not observe any clear pattern that would indicate shear thinning.

Rectangular boundary conclusion

We simulated a flow induced by a velocity prescribed on the upper boundary. In the problem with a still initial condition, the apparent viscosity is difficult to compare between different boundary velocities due to the inconsistency of the initial acceleration of the mixture. To address this issue, we prescribed a linear velocity profile as the initial condition with the aim to observe the apparent viscosity at the beginning of the simulation. However, the apparent viscosity varies in time significantly and no clear trend can be observed. The ideal solution

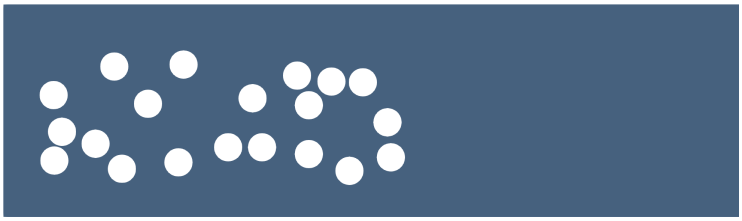

Figure 4.6: Initial random particle cluster used in the problem with linear initial velocity profile with 20 particles. The domain is more narrow than in the problem with stationary initial condition. In the problem with 40 particles, the initial cluster is wider. In the case of the particles in a grid, we used a 5×4 and 10×4 grid.

to this problem would be averaging the apparent viscosity over longer periods of time, which is impossible with the problem formulations used in this section as the particle distribution changes significantly in time.

The obvious solution to this problem would be the introduction of a periodic domain. However, our method is not well suited for periodic problems and the implementation would be rather difficult. The difficulty with periodic domains is the movement of particles through the boundary with the periodic boundary condition. We would need to remesh in each time step during the transition as well as keep track of the ball position on both sides. Although, this approach would be valid, we show a simpler solution in the following section.

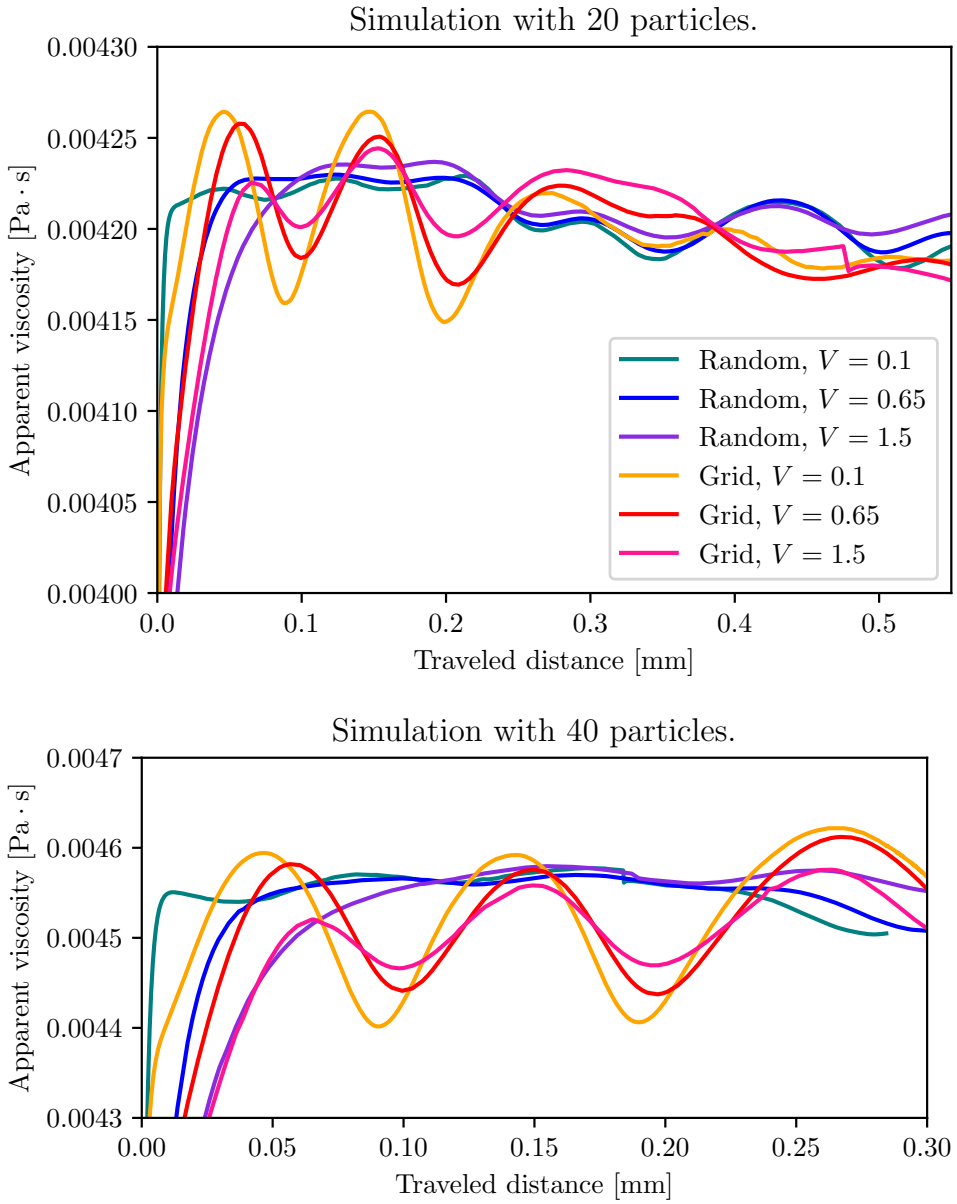

Figure 4.7: The dependence of the apparent viscosity as defined by (4.3) on time for the problem with linear profile as initial condition. There is a difference in behavior for uniformly distributed particles and particles in a grid. However, the apparent viscosity changes significantly with time and no clear shear thinning can be observed.

4.2 Flow between two cylinders

To extend the range of particle movement without the introduction of periodic domains, we use a domain defined as an area between two concentric circles with the particles orbiting around. This problem can be understood as a flow between two cylinders infinitely long in the direction of z-axis, but as the solution does not depend on z the two views are equivalent. We are still interested in a flow induced by prescribed velocity on the outer circle. Let us denote the outer circle by Γ_{O} and the inner circle by Γ_{I} as shown in Figure 4.8.

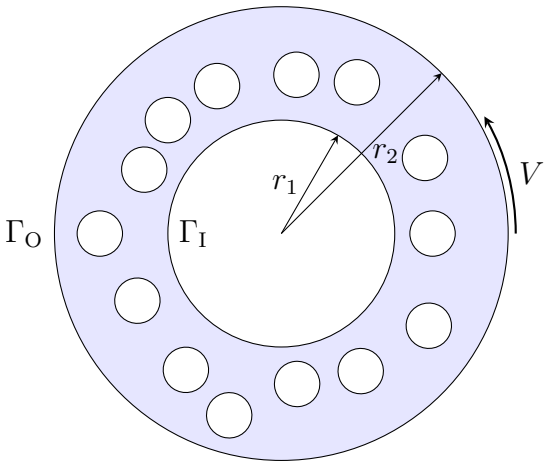

Figure 4.8: Domain used for the fluid flow problem between two concentric circles, the particles start randomly distributed in the space between the circles.

4.2.1 Apparent viscosity definition

The apparent viscosity definition for a problem of flow between two cylinders is analogous to the previous problem of flow between two planes. The main idea of our definition is to find a formula for viscosity using a solution of the problem with a Newtonian fluid. As the problem is slightly more intricate than in previous case, we present the whole process of obtaining the analytical solution.

The polar coordinates are a natural choice for this problem, we therefore start with the formulation of the Navier-Stokes equations (1.1)-(1.3) in polar coordinates. Let us denote the distance from the origin by $r \geq 0$ and the signed angle from the unit vector in the direction of the positive x-axis by $\theta \in [-\pi, \pi)$. We a priori assume that the solution does not depend on θ. In particular, we assume the velocity to be in a form

$$\mathbf{v}(r, \theta) = (0, v_\theta(r)).$$

With this assumption, the continuity equation is automatically satisfied. In the ballance of linear momentum equation, let us first calculate the velocity gradient in polar coordinates

$$\nabla \mathbf{v} = \begin{pmatrix} \frac{\partial v_r}{\partial r} & \frac{1}{r}\frac{\partial v_r}{\partial \theta} - \frac{v_\theta}{r} \\ \frac{\partial v_\theta}{\partial r} & \frac{1}{r}\frac{\partial v_\theta}{\partial \theta} + \frac{v_\theta}{r} \end{pmatrix} = \begin{pmatrix} 0 & -\frac{v_\theta}{r} \\ \frac{\partial v_\theta}{\partial r} & 0 \end{pmatrix}.$$

The convective term is reduced to the following form

$$(\mathbf{v}\cdot\nabla)\mathbf{v} = \begin{pmatrix} -\frac{1}{r}v_\theta^2 \\ 0 \end{pmatrix}, \tag{4.4}$$

and the Cauchy stress tensor reduces to the following form

$$\mathbb{T} = -p\mathbb{I} + \mu \begin{pmatrix} 0 & \frac{\partial v_\theta}{\partial r} - \frac{v_\theta}{r} \\ \frac{\partial v_\theta}{\partial r} - \frac{v_\theta}{r} & 0 \end{pmatrix}. \tag{4.5}$$

Expressions (4.4) and (4.5) substituted to the balance of linear momentum lead to the following two equations

$$\begin{aligned} \frac{\rho}{r}v_\theta^2 &= \frac{\partial p}{\partial r}, \\ \frac{\partial}{\partial r}\left(\frac{\partial v_\theta}{\partial r} - \frac{v_\theta}{r}\right) + \frac{2}{r}\left(\frac{\partial v_\theta}{\partial r} - \frac{v_\theta}{r}\right) &= 0. \end{aligned}$$

Using the first equation, pressure p is obtained directly from the the velocity field. However, we are more interested in the second equation, let us reorder the equation to see the structure more clearly

$$\frac{\partial^2 v_\theta}{\partial r} + \frac{1}{r}\frac{\partial v_\theta}{\partial r} - \frac{v_\theta}{r^2} = 0.$$

We deal with the Euler equation, where the general solution is in form

$$v_\theta = ar - b\frac{1}{r}, \tag{4.6}$$

where the coefficients $a, b \in \mathbb{R}$ are determined by the boundary conditions. The boundary conditions that the solutions should satisfy are the following

$$v_\theta(r_1) = 0, \qquad v_\theta(r_2) = V.$$

We can now substitute solution (4.6) into the boundary conditions and solve for a and b, this results in

$$\begin{aligned} a &= \frac{r_2}{r_2^2 - r_1^2}V, \qquad b = -\frac{r_1^2 r_2}{r_2^2 - r_1^2}V, \\ v_\theta(r) &= \frac{V r_2}{r_2^2 - r_1^2}\left(r - r_1^2\frac{1}{r}\right). \end{aligned}$$

Analogously to the previous section, we calculate the total force acting on the boundaries in the tangential direction. However, as the domain is circular, it is more convenient to use moment of force M instead of force. Let us calculate this moment for general circular boundary with the radius r and outward facing normal vector

$$M(r) = \int_0^{2\pi} r^2 T_{r\theta}\, d\theta = 2\pi\mu r^2\left(\frac{\partial v_\theta}{\partial r}(r) - \frac{v_\theta(r)}{r}\right) = 2\pi\mu\frac{r_1^2 r_2 V}{r_2^2 - r_1^2}. \tag{4.7}$$

Similarly to the previous example we take the sum of the moments on both boundaries

$$M(r_1) + M(r_2) = 4\pi\mu \frac{r_1^2 r_2 V}{r_2^2 - r_1^2}.$$

This leads to the following choice of apparent viscosity for our problem.

$$\mu_{\text{app}} = \frac{r_2^2 - r_1^2}{r_1^2 r_2} \frac{M(r_1) + M(r_2)}{4\pi V}. \tag{4.8}$$

To finish the computation, we show a way to numerically obtain $M(r)$ from the Cauchy stress tensor, as we have the solution in Cartesian coordinates by default. The moment calculation can be easily simplified for $r = |\mathbf{x}| = r_1, r_2$ using the fact that the unit outer normal vector of a circular boundary is $\mathbf{n} = \frac{\mathbf{x}}{|\mathbf{x}|} = \mathbf{e}_r(\mathbf{x})$. In particular, we obtain the following identity for the Cauchy stress tensor

$$\mathbb{T}_{r\theta} = \mathbf{e}_\theta \cdot \mathbb{T}\mathbf{e}_r = \mathbf{n} \times \mathbb{T}\mathbf{n}.$$

We used the property of the vector $\mathbf{e}_\theta = \frac{1}{r}\frac{\partial \mathbf{x}}{\partial \theta}$

$$\mathbf{e}_\theta = \frac{1}{r}(-y, x), \quad \mathbf{e}_\theta \cdot \mathbf{y} = \mathbf{n} \times \mathbf{y} \quad \forall \mathbf{y} \in \mathbb{R}^2.$$

Using this identity and the equation (4.7), we obtain the following identity for a circular boundary Γ with radius r

$$M(r) = \int_0^{2\pi} r^2 T_{r\theta}\, d\theta = \int_0^{2\pi} r\mathbf{n} \times \mathbb{T}(r\mathbf{n})\, d\theta = \frac{1}{r}\int_\Gamma \mathbf{x} \times \mathbb{T}\mathbf{x}\, d\mathbf{x}.$$

4.2.2 Numerical results

For this problem, we chose the same fluid parameters values as in the previous case, the size of domain Ω is defined by

$$r_1 = 30\,\mu\text{m}, \quad r_2 = 60\,\mu\text{m}.$$

The initial condition is chosen as zero movement for both the fluid and every particle. We prescribe the velocity on the outer boundary to be a vector of magnitude V in the tangent direction to the boundary, more specifically

$$\mathbf{v} = \frac{V}{\sqrt{x^2 + y^2}} \begin{pmatrix} -y \\ x \end{pmatrix} \quad \text{on } \Gamma_{\text{O}}.$$

A slight problem with the circular domain is caused by the way we move the particles in our method. The motion of particle is computed using the explicit Euler method, see 2.21. In particular, if we have a particle in a circular domain with a fluid moving purely in tangential direction. Neglecting the effect a particle has on the fluid, the particle should move in a circular trajectory. However, if we use an explicit method, the particle will systematically drift away from the center due to numerical error as shown in Figure 4.9. The effect is less significant with smaller time step size, but for a long simulation may cause a collision between particle and the outer wall. To address this problem without creating additional

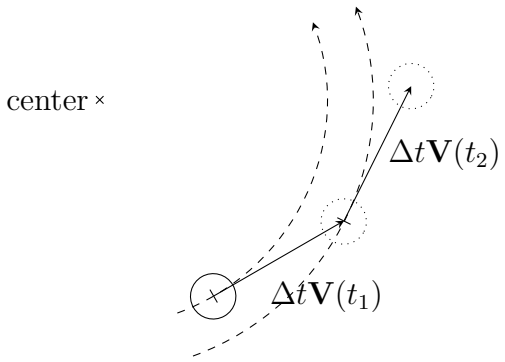

Figure 4.9: Numerical approximation of a particle movement on a circular trajectory results in a systematic drift of the particle away from the center of rotation. Dashed line represents the expected trajectory, the arrow represents the real movement of the particle with the use of an explicit numerical method.

computational complexity, we choose the particle density slightly lower than the fluid density.

$$\rho_{\text{particle}} = 1010\,\frac{\text{kg}}{\text{m}^3}.$$

Similarly to the problem with the rectangular domain, the boundary condition (2.18) for mesh velocity is a bad choice. As the particles move near the stationary boundary with relatively large speed, the mesh would become deformed. However, unlike in the previous problem, a simple $\mathbf{v}_{\text{mesh}} \cdot \mathbf{n} = 0$ on Γ_{O} is not sufficient due to more complicated geometry. We therefore prescribe the boundary condition similar to (2.19):

$$\mathbf{v}_{mesh} = \frac{1}{\Delta t}\begin{pmatrix}\cos(\Delta t\,\omega) - 1 & -\sin(\Delta t\,\omega)\\ \sin(\Delta t\,\omega) & \cos(\Delta t\,\omega) - 1\end{pmatrix}\mathbf{x} \quad \text{on } \partial\Omega_O. \tag{4.9}$$

The angular velocity ω is chosen to be close to the angular velocity of the fastest particle, in our case

$$\omega = r_2 \max\left\{|\mathbf{V}_i|, i = 1, ..., N\right\}.$$

The same problem may occur near the inner boundary, we prescribe (4.9) on Γ_{I} with

$$\omega = r_1 \min\left\{|\mathbf{V}_i|, i = 1, ..., N\right\}.$$

We ran the simulation for multiple count of particles and we obtained the best results for 20 particles as we are able to compute long simulations with enough particle interactions. For 40 and more particles, the viscosity significantly varies in time, which makes the viscosity comparison rather difficult. Moreover, the simulation gets relatively expensive as we have to use a small time step to capture particle interactions and avoid collisions. The apparent viscosity for 20 particles is shown in Figure 4.11 and Table 4.1. We can clearly see that the average viscosity of a run with a larger velocity is smaller than of the one with smaller velocity, which can be interpreted as the effect of shear thinning. We also know, that this effect is not caused by faster development of higher velocity system, as we observe the values based on a traveled distance rather than passed time.

Velocity V $[\frac{\mathrm{m}}{\mathrm{s}}]$	0.1	0.65	1.5
Apparent viscosity $[10^{-3}\,\mathrm{Pa}\cdot\mathrm{s}]$	5.429	5.289	5.181

Table 4.1: The average apparent viscosity on interval $(0\,\mathrm{mm}, 2.3\,\mathrm{mm})$ of traveled distance. The result for each velocity are obtained as averages over 2 runs with different initial particle distributions.

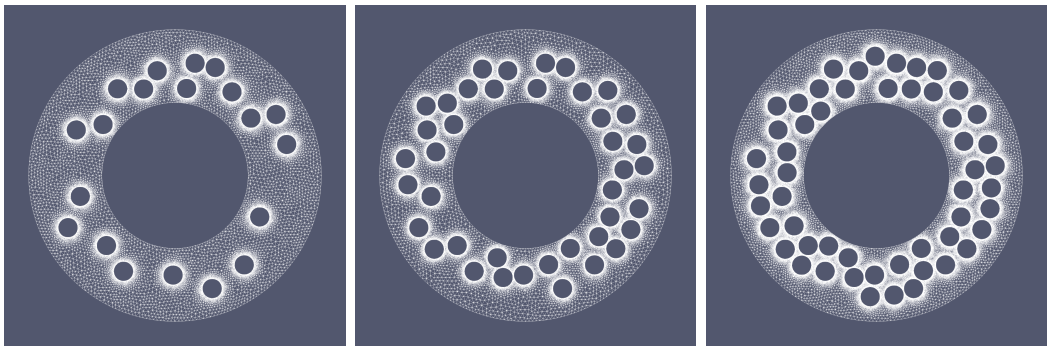

Figure 4.10: The initial particle distribution and mesh density in a problem of flow between two circles with 20 (left), 40 (middle) and 53 (right) particles.

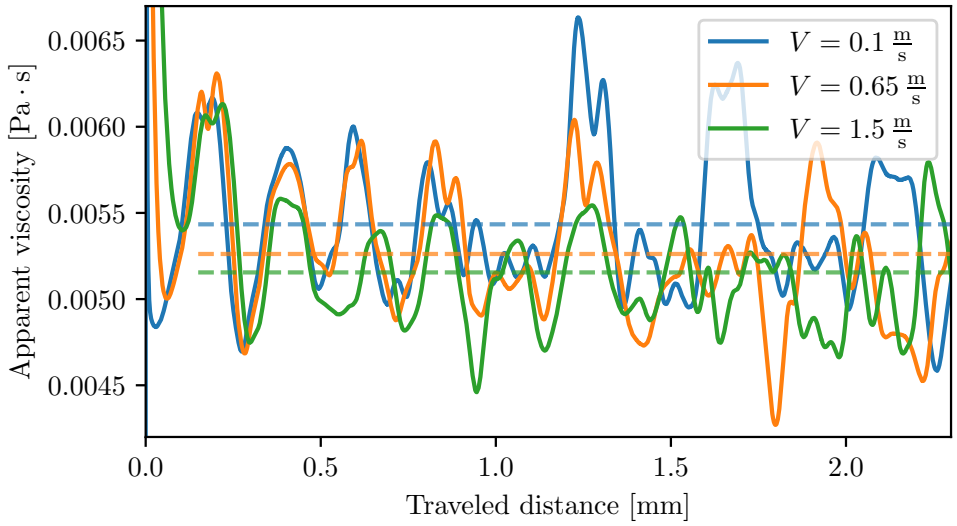

Figure 4.11: The dependence of the apparent viscosity on traveled distance for a problem in circular domain with 20 circular particles with common initial particle distribution (random seed). The dashed line represents the average value over interval $(0.15\,\mathrm{mm}, 2.3\,\mathrm{mm})$. Although the pattern is not as obvious in the raw values, the shear thinning effect can be clearly seen in the averages.

Conclusion

In this thesis, we developed a numerical model based on the arbitrary Lagrangian-Eulerian (ALE) method to study a system of rigid particles in a Newtonian fluid. The main motivation was to study the interaction individual components and resulting response of the mixture as a whole.

The ALE method was initially presented on a simple example of a fluid flow around a sphere in an infinite domain. We were able to replicate the Stokes formula for drag with a numerical method based on a boundary moving with a fixed velocity. The approximation obtained from ALE method was comparable to a more standard approach of using a stationary domain with prescribed fluid velocity in large distance from the particle. We observed only a slightly increased sensitivity to the numerical parameters.

To simulate a more complicated system, a more robust method to simulate the full two-way coupling between fluid and particles was used. We described the main issues connected with implementation of this method, namely the problems emerging from the mesh movement leading to the necessity to remesh and the intricacies of prescribing the boundary condition on particle surfaces for both the fluid movement and mesh movement.

The resulting method is capable of simulating tens of rigid particles. Most examples consider circular particles for computational simplicity, but an example with elliptical particles was also presented. The method was tested on various benchmarks that confirmed the reliability of the method. In particular, the model captures the interaction of very heavy particles correctly. We were also able to replicate the theoretical behavior of a particle approaching a flat surface with fairly good numerical accuracy. On top of that, the conservation of both angular and linear momentum was confirmed.

As the major point of interest, a shear thinning was calculated in problems inspired by the blood flow. We initially formulated a problem with particles in a rectangular domain with prescribed shear strain. An increase of apparent viscosity with particle count was observed as well as the dependence of apparent viscosity on particle distribution. However, no shear thinning was observed. To study the system over longer periods of time, a problem of flow between two cylinders was used, which resulted in a clear example of shear thinning. We showed that the effective viscosity of the mixture of a Newtonian fluid and rigid particles is higher than the viscosity of the pure Newtonian fluid. Furthermore, the mixture as a whole effectively behaves as a shear thinning fluid.

Bibliography

M. Brdička. *Mechanika kontinua*. Česká matice technická ; roč. 110, č. spisu 503. Academia, Praha, vyd. 3., rev. edition, 2005. ISBN 80-200-1344-X.

R. Chabiniok, J. Hron, A. Jarolímová, J. Málek, K.R. Rajagopal, K. Rajagopal, H. Švihlová, and K. Tůma. A benchmark problem to evaluate implementational issues for three-dimensional flows of incompressible fluids subject to slip boundary conditions. *Applications in Engineering Science*, 6:100038, jun 2021. doi: 10.1016/j.apples.2021.100038.

J. Donea, A. Huerta, J.-Ph. Ponthot, and A. Rodríguez-Ferran. *Arbitrary Lagrangian–Eulerian Methods*, chapter 14. John Wiley & Sons, Ltd, 2004. ISBN 9780470091357. doi: https://doi.org/10.1002/0470091355.ecm009.

J. Fara. ADmesh. `https://bitbucket.org/FaraJakub/admesh/src/master/`, 2022.

G. Gravina, S. Schwarzacher, O. Souček, and K. Tůma. Contactless rebound of elastic bodies in a viscous incompressible fluid. *Journal of Fluid Mechanics*, 942:A34, 2022. doi: 10.1017/jfm.2022.243.

H. H. Hu, N.A. Patankar, and M.Y. Zhu. Direct numerical simulations of fluid–solid systems using the arbitrary Lagrangian–Eulerian technique. *Journal of Computational Physics*, 169(2):427–462, 2001. ISSN 0021-9991. doi: https://doi.org/10.1006/jcph.2000.6592.

T. J.R. Hughes, W. K. Liu, and T. K. Zimmermann. Lagrangian-Eulerian finite element formulation for incompressible viscous flows. *Computer Methods in Applied Mechanics and Engineering*, 29(3):329–349, dec 1981. doi: 10.1016/0045-7825(81)90049-9.

L. Lanotte, J. Mauer, S. Mendez, D. A. Fedosov, J. Fromental, V. Claveria, F. Nicoud, G. Gompper, and M. Abkarian. Red cells' dynamic morphologies govern blood shear thinning under microcirculatory flow conditions. *Proceedings of the National Academy of Sciences*, 113(47):13289–13294, nov 2016. doi: 10.1073/pnas.1608074113.

L. Gary Leal. Chapter 7 - thin films, lubrication, and related problems. In L. Gary Leal, editor, *Laminar Flow and Convective Transport Processes*, pages 345–448. Butterworth-Heinemann, Boston, 1992. ISBN 978-0-7506-9117-8. doi: https://doi.org/10.1016/B978-0-7506-9117-8.50014-7.

A. Lefebvre and B. Maury. Apparent viscosity of a mixture of a Newtonian fluid and interacting particles. *Comptes Rendus Mécanique*, 333(12):923–933, dec 2005. doi: 10.1016/j.crme.2005.10.007.

A. Leuprecht and K. Perktol. Computer Simulation of Non-Newtonian Effects on Blood Flow in Large Arteries. *Computer Methods in Biomechanics and Biomedical Engineering*, 4(2):149–163, jan 2001. doi: 10.1080/10255840008908002.

J. Nitsche. Über ein variationsprinzip zur lösung von dirichlet-problemen bei verwendung von teilräumen, die keinen randbedingungen unterworfen sind. *Abhandlungen aus dem Mathematischen Seminar der Universität Hamburg*, 36 (1):9–15, jul 1971. doi: 10.1007/bf02995904.

M. Schäfer, S. Turek, F. Durst, E. Krause, and R. Rannacher. *Benchmark Computations of Laminar Flow Around a Cylinder*. Vieweg+Teubner Verlag, 1996. doi: 10.1007/978-3-322-89849-4_39.

J. Trdlicová. Blood flow modeling in cerebral aneurysm. Master's thesis, Charles University, Faculty of Mathematics and Physics, 2021.

R. Verfürth. Error estimates for a mixed finite element approximation of the stokes equations. *RAIRO. Analyse numérique*, 18(2):175–182, 1984. doi: 10.1051/m2an/1984180201751.

D. Wan and S. Turek. Direct numerical simulation of particulate flow via multigrid FEM techniques and the fictitious boundary method. *International Journal for Numerical Methods in Fluids*, 51(5):531–566, 2006. doi: 10.1002/fld.1129.